Nanoscale

ROYAL SOCIETY OF CHEMISTRY

MINIREVIEW

View Article Online
View Journal | View Issue

Cite this: *Nanoscale*, 2024, **16**, 7841

Lattice engineering of noble metal-based nanomaterials *via* metal–nonmetal interactions for catalytic applications

Long Zheng,† Lei Xu,† Ping Gu† and Ye Chen *

Received 6th February 2024,
Accepted 15th March 2024

DOI: 10.1039/d4nr00561a

rsc.li/nanoscale

Noble metal-based nanomaterials possess outstanding catalytic properties in various chemical reactions. However, the increasing cost of noble metals severely hinders their large-scale applications. A cost-effective strategy is incorporating noble metals with light nonmetal elements (*e.g.*, H, B, C, N, P and S) to form noble metal-based nanocompounds, which can not only reduce the noble metal content, but also promote their catalytic performances by tuning their crystal lattices and introducing additional active sites. In this review, we present a concise overview of the recent advancements in the preparation and application of various kinds of noble metal–light nonmetal binary nanocompounds. Besides introducing synthetic strategies, we focus on the effects of introducing light nonmetal elements on the lattice structures of noble metals and highlight notable progress in the lattice strain engineering of representative core–shell nanostructures derived from these nanocompounds. In the meantime, the catalytic applications of the light element-incorporated noble metal-based nanomaterials are discussed. Finally, we discuss current challenges and future perspectives in the development of noble metal–nonmetal based nanomaterials.

1. Introduction

Noble metal-based nanomaterials possess outstanding catalytic properties, including activity, selectivity, and durability, in a variety of catalytic reactions,[1–4] which are important for developing sustainable energy storage and conversion technologies to mitigate global energy crisis and environmental pollution.[5–7] For example, noble metal based electrocatalysts play key roles in proton exchange membrane fuel cells, which are promising clean energy conversion devices due to their high efficiency, high power density and low pollution emission.[8,9] However, the low abundances and ever-increasing prices of noble metals still inhibit their commercial applications. Numerous strategies have been developed to fine-tune the noble metal-based nanostructures, including size,[10] shape/facet,[11] and composition control,[12,13] to enhance their intrinsic catalytic properties and facilitate their sustainable use. Among these strategies, alloying noble metals with other elements to form nanoalloys or nanocompounds stands out as one of the most effective approaches to simultaneously reduce noble metal consumption, modify their electronic structure, and promote their catalytic properties.[14,15]

Particularly, compared with the intensively studied metal–metal alloys, the incorporation of light nonmetal elements to form metal–nonmetal alloys or compounds has garnered increasing attention in the past decades because of several advantages.[12,16] First, nonmetal elements have a wider range of electronegativities, which can lead to a variety of metal–nonmetal interactions that are covalent, metallic, or ionic. Second, a simultaneous change of the lattice structure, including strain and symmetry, of host noble metals could take place, causing local lattice distortion or even phase transformation.

Department of Chemistry, The Chinese University of Hong Kong, Hong Kong, China. E-mail: yechen@cuhk.edu.hk
† These authors contributed equally to this work.

Ye Chen

Dr Ye Chen is currently an assistant professor at the Department of Chemistry, The Chinese University of Hong Kong. She received her B. Eng. and Ph.D. degrees (Supervisor: Prof. Hua ZHANG) in materials science from Nanyang Technological University (Singapore) in 2015 and 2019, respectively. Her current research interest focuses on wet-chemical synthesis of novel low-dimensional nanomaterials and their applications in catalysis and clean energy.

Depending on the insertion pathway, there are two common types of light nonmetal incorporation strategies in the noble metal.[17] Lighter elements with smaller atomic radii, such as hydrogen (H), boron (B), carbon (C), and nitrogen (N), tend to occupy interstitial sites in the host metal, while for elements with larger atomic/ionic radii, such as phosphorus (P) and sulfur (S), they can also substitute the host atoms to constitute alloys or nanocompounds. Consequently, the binary nano-alloys or nanocompounds may exhibit distinct lattice strain or altered symmetry compared to the parent metal lattice (Fig. 1). Importantly, these modifications of the lattice structure of nanomaterials could affect their physicochemical properties and eventually impact their catalytic performances.[18–20] Third, the abundant reserves of most light nonmetal elements make it cost-effective to develop noble metal–light nonmetal based nanomaterials.

Strategies to achieve the incorporation of light nonmetal elements can be divided into two main categories, *i.e.* wet chemical methods and high-temperature solid-state methods. Compared with the harsh conditions in solid-state methods,[21,22] wet chemical methods possess attractive advantages, including accurate control over the morphology and composition,[23,24] more flexible synthetic routes for complex nano-architechtures,[25,26] as well as good scalability. In the meantime, besides synthesis methods, the recent development of advanced characterization techniques, such as aberration-corrected transmission electron microscopy (TEM), neutron powder diffraction (NPD), extended X-ray absorption fine structure (EXAFS) spectroscopy, and X-ray absorption near-edge structure (XANES) spectroscopy, allows us to better understand the structure–property relationship and further optimize the nanostructures towards enhanced catalytic properties.

In this mini-review, we present an overview of the recent progress in the controlled synthesis, characterization, and catalytic performances of various noble metal-based nanomaterials, whose lattices were engineered by incorporating H, B, C, N, P, or S *via* wet chemical methods. We classify strategies to achieve the lattice engineering of noble metal-based nanomaterials into two categories: direct lattice engineering and indirect lattice engineering. First, in the direct lattice engineering, representative studies of lattice strain and symmetry engineering of various noble metal-based nanocompounds, including noble metal hydrides, borides, carbides, nitrides, phosphides and sulfides, and their catalytic performances are introduced. Then, typical examples of indirect lattice engineering *via* the formation of core–shell heterostructures are presented. Finally, some major challenges, opportunities and future directions in this emerging research field are discussed.

2.1. Direct lattice engineering of noble metal–light nonmetal nanocompounds

Based on the types of light nonmetal elements incorporated, in this section, we focus on lattice engineering of binary nanocompounds including noble metal hydrides, borides, carbides, nitrides, phosphides, and sulfides. Since the inserted light nonmetals may directly alter both lattice strain and symmetry of the host noble metals, we will separately discuss the strain and symmetry effects caused by the formation of these nanocompounds in two sections.

2.1.1. Lattice strain engineering. Lattice strain generally refers to the change in the bond length on a particle surface or in a localized region compared with the initial bond length in bulk materials.[27] Modulating lattice strain in metal-based nanomaterials has been recognized as a powerful method to improve their catalytic performance.[20] To date, many strategies have been developed to induce lattice strain in metal nanomaterials, such as introducing supports[28] or defects,[29] alloying with second metals,[30] precise morphology control,[31] and so on. Different from these strategies, the incorporation of light nonmetal elements into the noble metal lattice could not only

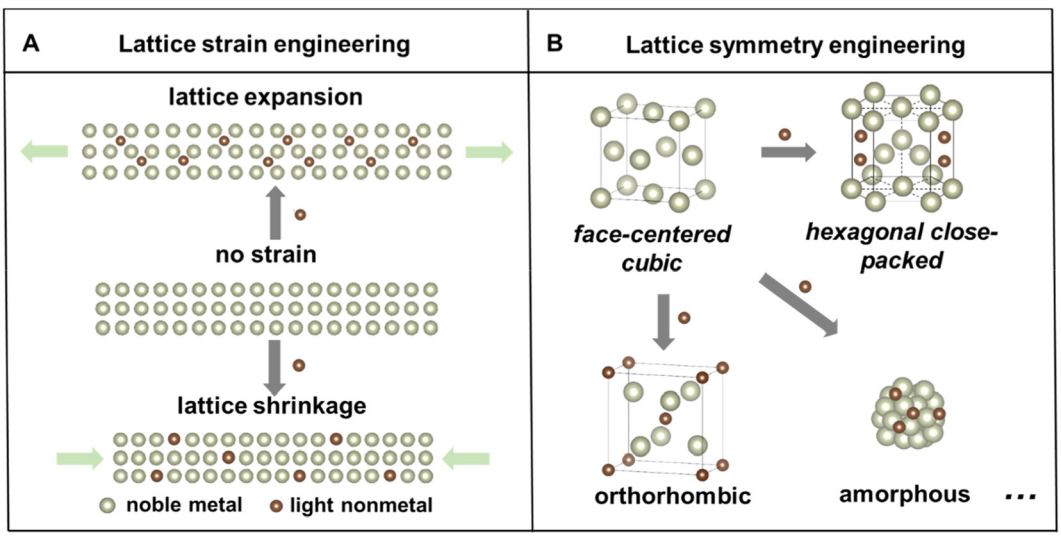

Fig. 1 Schematic illustrations of lattice engineering of noble metal–light nonmetal binary nanocompounds *via* (A) lattice strain engineering and (B) lattice symmetry engineering from an fcc host metal.

induce tensile or compressive lattice strain (Fig. 1A), but also tune the electronic structures of noble metals due to their very different electronegativities. In this section, we present representative works of the lattice strain engineering of noble metal binary nanocompounds *via* incorporating light nonmetal elements.

Noble metal hydrides. Noble metal hydrides are key candidates in many catalytic reactions.[14,16] H, as the smallest atom, can be easily incorporate into octahedral or tetrahedral interstitial sites of noble metal lattices, resulting in the formation of metal-H bonds and metal lattice expansion,[32–35] The electrons from H atoms could directly contribute to a higher electron density of the host metal and therefore affect its physicochemical properties.[36] In the meantime, the tensile strain caused by the expanded lattice can lead to the narrowing and center upshift the d-band of the host metal,[37] which could be beneficial for improving the catalytic properties.[38–41]

To date, wet chemical preparation of noble metal hydrides only succeeded in the preparation of palladium hydride (PdH_x)[42,43] and rhodium hydride[44] possibly due to their high affinity differences.[45] The face-centered cubic (fcc) PdH_x normally exists in two phases, depending on its H content (x). One is the α phase ($0 < x < 0.02$), in which the H atoms only slightly diffuse into Pd and cause lattice expansion. The other one is the β phase ($0.6 < x < 1$), in which the Pd lattice is inserted by more H atoms and further expanded. Sometimes, α and β phases can coexist in PdH_x ($0.02 \leq x \leq 0.6$) nanocrystals.[46,47] In general, the H interstitial sites are determined by the ratio of H/Pd in the Pd–H system, which can be derived from the lattice parameter of the PdH_x nanocompounds.[48–50] To distinguish the slight changes in lattice parameters of different PdH_x, advanced characterization techniques, like aberration-corrected high-angle annular dark-field scanning transmission electron microscopy (HAADF-STEM) and X-Ray diffraction (XRD) analysis, are often required.

The wet chemical preparation of PdH_x nanocrystals often starts from pre-synthesized Pd nanocrystals, followed by H intercalation. The choice of a suitable H precursor is critical. Besides H_2, H-containing chemicals that readily release H_2 can also act as H sources, including sodium borohydride ($NaBH_4$), hydrazine (N_2H_4), *n*-butylamine, and *N*,*N*-dimethylformamide (DMF). For example, the $NaBH_4$-based thermal treatment method was used to synthesize PdH_x nanocrystals by Phan *et al.*[51] Specifically, pre-synthesized Pd nanocrystals and $NaBH_4$ were dispersed in tetraethylene glycol solution, in which Pd further reacted with $NaBH_4$ during heating to form PdH_x. Compared with pure Pd nanocrystals, the PdH_x samples prepared at different temperatures (from 90 °C to 190 °C) showed XRD peak shifts to lower 2θ angles (Fig. 2A). It worth mentioning that β-$PdH_{0.7}$ could be obtained from Pd nanocrystals at reaction temperatures over 120 °C, while for bulk Pd, complete conversion of Pd to β-$PdH_{0.7}$ occurred only at 190 °C.

Different from $NaBH_4$, some organic molecules like DMF and *n*-butylamine release H_2 by reacting with Pd surface to finally form PdH_x. *Via* the organic molecule-based thermal method, shape-controlled synthesis of PdH_x has been investigated. For instance, $PdH_{0.43}$ nanopolycrystals, nanotetrahedra and nanocubes were synthesized by treating the corresponding Pd nanocrystals in DMF solution at 160 °C for 16 h.[23] All XRD diffraction peaks of the three final $PdH_{0.43}$ products shifted to lower angles with respect to those of original Pd nanocrystals, which proved the expansion of Pd lattice and successful incorporation of H atoms into Pd lattices (Fig. 2B–D). The $PdH_{0.43}$ nanopolycrystals and $PdH_{0.43}$ nanotetrahedra exhibited higher catalytic activities than their counterparts in the methanol oxidation reaction (MOR). Adopting the same two-step strategy, PdH_x nanodendrites were synthesized by heating the pre-prepared Pd nanodendrites in DMF solution at 160 °C for 20 h.[52] Compared with commercial Pd nanocrystals and Pd nanodendrites, PdH_x nanodendrites showed enhanced electrocatalytic activities for both the formic acid oxidation reaction (FAOR) and hydrogen evolution reaction (HER). The authors applied theoretical analysis to show that PdH_x may have weaker binding energies of intermediate catalytic species and toxic CO due to the ligand effect, which led to its higher catalytic activity. Besides shape controlled PdH_x nanocrystals with a tunable H content of up to 0.43 have also been realized by the organic molecule-based thermal method. For example, a series of PdH_x nanocatalysts with different H contents from 0.10 to 0.43 could be synthesized by heating the commercial Pd black in *n*-butylamine from 80 °C to 200 °C.[53] The authors supposed that H_2 was released by *n*-butylamine, a process catalyzed *via* Pd black. Then, H_2 was adsorbed and dissociated on the Pd surface, enabling H diffusion into interstitial sites of the Pd lattice. The lattice distance (0.23 nm) of H-incorporated Pd $(111)_f$ nanoparticle were directly observed by high resolution TEM (HRTEM) to be larger than that of fcc Pd (0.22 nm) (Fig. 2E), proving the successful incorporation of H with an estimated content of 0.43.[48,54] Compared with commercial Pd black and PdH_x with other stoichiometries (0.10, 0.29, and 0.33), the $PdH_{0.43}$ nanocatalysts showed lower overpotential, higher mass activity and better catalytic stability towards FAOR. The authors claimed that the excellent performance could be attributed to the weakened binding interactions between PdH_x and reaction intermediates.

Another interesting aspect is to understand the phase transformation behavior of PdH_x nanocrystals. It is commonly observed that the transformation of α-phase PdH_x to β-phase PdH_x, starts from the nucleation of the β-phase at the vertices of the nanocrystals, which then spreads to the whole nanocrystal.[38] However, the process is considered difficult because the high energetic α/β phase interface is thermodynamically unfavorable for the formation of PdH_x with intermediate α/β ratios, which often prevents the final formation of β-phase PdH_x.[38] Interestingly, a recent work reported a different transformation pathway. Zhou *et al.* found that the morphology of Pd nanocrystals could affect the transformation pathway of Pd to PdH_x when using N_2H_4 as the H source.[55] They observed that the Pd nano-icosahedron could transform into PdH_x ($0 < x \leq 0.7$) *via* a "single-phase pathway", while Pd nano-octahedra with a similar size experienced a "two-phase pathway" to PdH_x ($0 < x$

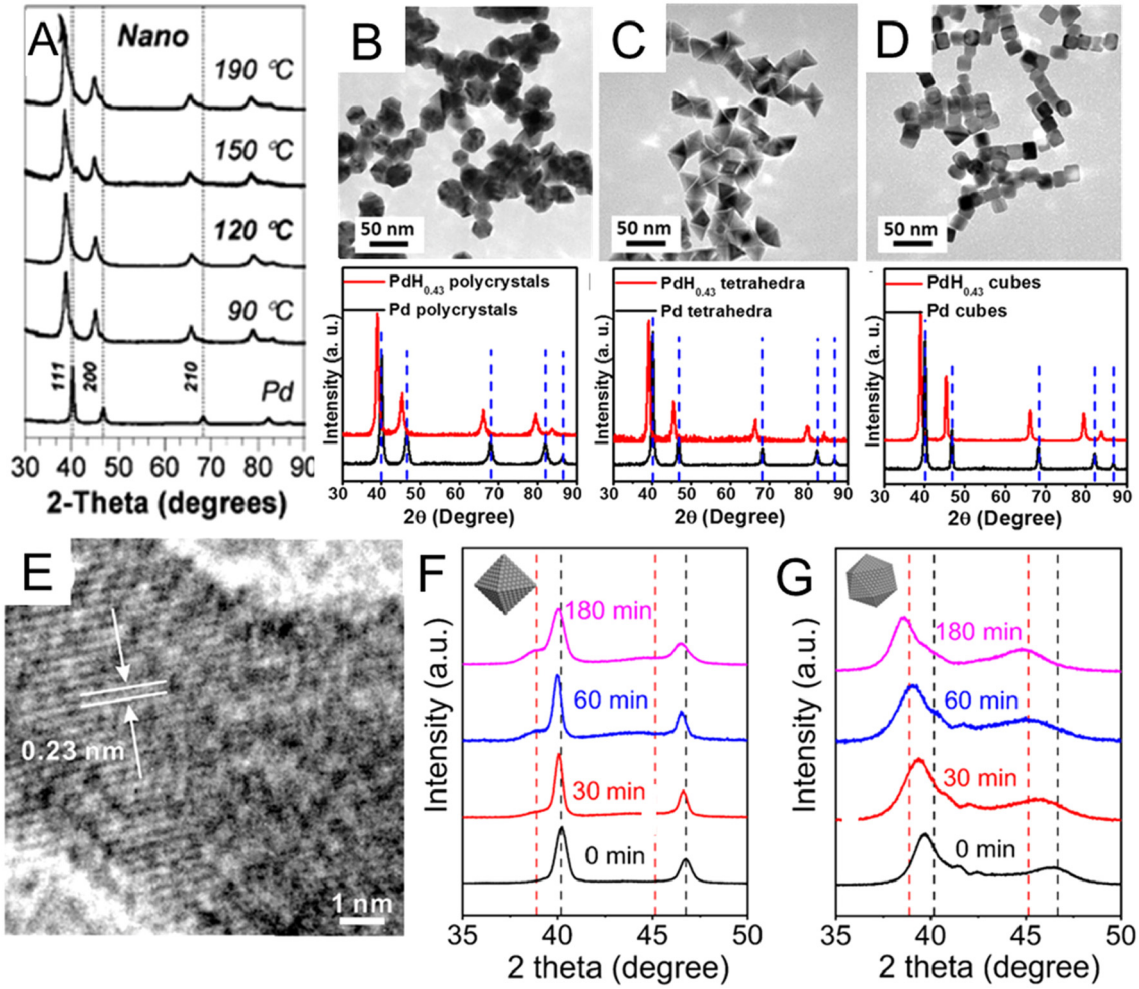

Fig. 2 (A) X-ray diffraction (XRD) patterns of lattice-engineered PdH_x nanocrystals. Vertical dashed lines indicate the peak positions of Pd. Reproduced with permission from ref 51 Copyright 2009, Royal Society of Chemistry. (B–D) Comparisons of transmission electron microscopy (TEM) images and XRD spectra of $PdH_{0.43}$ (B) nanopolycrystals, (C) nanotetrahedra, and (D) nanocubes before and after conversion. Reproduced with permission from ref 23. Copyright 2015, American Chemical Society. (E) High resolution TEM (HRTEM) image of a typical $PdH_{0.43}$ nanocrystals showing larger lattice distances than Pd. Reproduced with permission from ref 53. Copyright 2017, Elsevier. XRD patterns of (F) Pd octahedral nanocrystals and (G) Pd icosahedral nanocrystals after different treating times by N_2H_4. The black and red dash lines indicate the positions of the peaks associated with fcc-Pd and the β-phase $PdH_{0.7}$, respectively. Reproduced with permission from ref 55. Copyright 2023, Wiley-VCH.

≤ 0.7) when treated by the same process. Specifically, the analyses of the XRD pattern showed that the Pd nano-octahedra were α phase at the initial stage. As the N_2H_4 treatment prolonged, a new $(111)_f$ peak belonging to the β-phase $PdH_{0.7}$ appeared at around 38.8°, indicating that the α phase partially converted to the β phase. The two phases coexisted throughout the treatment, known as the "two-phase pathway" (Fig. 2F). As for Pd nano-icosahedra, after treatment with N_2H_4 for the same period of time, the Pd $(111)_f$ peak at about 39.84° from Pd nano-icosahedra left shifted continuously (without splitting into two peaks) until 38.46°, indicating that the PdH_x icosahedral nanocrystals experienced a "single-phase pathway". The H/Pd ratio increased with treatment time and reached 0.7. (Fig. 2G). Note that the icosahedral Pd nanoseeds may possess higher internal lattice strain than octahedral Pd, as indicated by the broader and left-shifted XRD peaks (Fig. 2F and G), which may still be preserved after incorporating H. As a possible result, the $PdH_{0.7}$ nano-icosahedra demonstrated higher catalytic activity and better catalytic stability toward FAOR than the $PdH_{0.7}$ nano-octahedra.

While PdH_x is the most reported noble metal hydrides, recently, ambient-stable rhodium hydride (RhH) nanosheets with around 1 nm thickness have been reported by Fan *et al.*[44] Different from the preparation of PdH_x, a one-pot solvothermal method was applied to synthesize ultrathin RhH nanosheets *via* reducing the Rh precursor in the mixed solution of *n*-butylamine, formaldehyde, and benzyl-alcohol at 160 °C. Note that *n*-butylamine, formaldehyde, and benzyl-alcohol could all serve as the H source. The expanded lattice spacing of RhH (2.36 Å) than that of Rh (2.25 Å) suggested the successful incorporation of H. The existence of H was confirmed by solid-state 1H nuclear magnetic resonance spectra and the atomic ratio

Rh/H was confirmed to be 1 : 1 by the well-fitted XRD pattern with standard RhH. Compared with commercial Pt/C (30 mV) and Rh nanosheets (57 mV), the RhH nanosheets exhibited excellent HER performance with a lower overpotential (28 mV) and better stability. Theoretical calculations showed that the interstitial H atoms in RhH nanosheets can modulate the adsorption energy of H intermediates and promote H_2 desorption to enhance HER activity.

Noble metal borides. B is located at the boundary between metals and nonmetals in the periodic table, which is well-known as a metalloid element with properties of both metals and nonmetals. Due to the unique electronic structure and small atomic radius of the B element, many different types of noble metal borides have been successfully synthesized *via* wet chemical methods by employing various B sources, including dimethylamine borane (DMAB), borane tetrahydrofuran (BH_3-THF) and $NaBH_4$.[56,57]

Organic B sources, including DMAB and BH_3-THF, are stable and gentle B-releasing agents commonly used in organic solvent-based synthesis.[58–60] In 2009, Wang *et al.* first developed a one-pot synthesis using DMAB to prepare B-doped Pd nanoparticles supported on carbon powder (PdB_x/C) in alkaline aqueous solution.[58] Importantly, in alkaline solutions, DMAB could react with OH^- to generate BH_3OH^-, which further served as both a reductant and a B source to reduce Pd (II) ions and then release B to form PdB_x.[61] The obtained PdB_x/C with 6.3 at% B content showed fcc Pd characteristic peaks with left shifts in the XRD pattern, indicating the expanded lattice distance in PdB_x/C due to the incorporation of B atoms. PdB_x/C showed enhanced activity and durability in catalyzing the formic acid electro-oxidation reaction than commercial Pd/C due to the electronic modification effect of B atoms. Then, the same group further expanded the application of the catalyst and applied the catalyst for formic acid decomposition reaction.[59] Compared with commercial and homemade Pd/C, PdB_x/C showed a much higher activity toward H_2 production, possibly because the enlarged Pd lattice in PdB_x (Fig. 3A) enhanced the adsorption of formate ions to reduce the activation energy of formic acid dehydrogenation. Due to the strong reduction ability of DMAB, the growth process is thermodynamically controlled, resulting in less morphology control of most reported PdB_x nanomaterials.[62–64] Therefore, other strategies, such as adding surfactants to control the reaction kinetics or adopting a two-step method to separate the nanocrystal growth and doping processes, have been developed to prepare PdB_x nanocrystals with controlled morphologies, such as nanowires and mesoporous nanospheres.[65,66] Recently, platinum (Pt) boride nanoparticles supported on carbon black (PtB_x/C) have also been reported by using DMAB as the reductant and the B source.[60] The content of B in PtB_x/C detected by inductively coupled plasma atomic emission spectroscopy (ICP-AES) was around 6.6 at%, causing around 2% expansion of the Pt lattice in the XRD pattern. HRTEM also directly observed the slightly larger lattice distance of $(111)_f$ in Pt–B/C (0.231 nm) than that in Pt/C (0.227 nm). Notably, as the oxygen reduction reaction (ORR) catalyst in the single H_2–O_2 fuel cell, the maximum power density of PtB_x/C was 1.24 times as high as that of Pt/C. Besides DMAB, BH_3-THF is another organic B source.[67,68] Since BH_3-THF is liquid, it can serve as both a B source and solvent during the B doping process. For instance, Chan *et al.* reported PdB_x/C with a high content of B (up to 20 at%) by heating Pd/C and BH_3-THF in a THF solution at 100 °C for 1 h under a H_2 atmosphere.[67] During heating, BH_3-THF would decompose to B_2H_6, catalyzed by Pd/C, and further release B atoms.[14] After doping, the obtained PdB_x/C maintained the fcc phase with 3.6% lattice expansion. EXAFS data showed that the insertion of B clearly led to an increase of the average Pd–Pd distance. Compared with Pd/C, PdB_x/C displayed much enhanced selectivity (98%) for partial hydrogenation of 3-hexyn-1-ol to *cis*-hexen-1-ol without over-hydrogenation products. Theoretical calculations showed that B atoms could occupy the H adsorption sites on the Pd surface and reduce undesirable over-hydrogenation.

As an inorganic boronizing reagent, $NaBH_4$ is a powerful B-source to synthesize a wide range of noble metal borides.[69–71] For instance, Li *et al.* developed a one-pot method to prepare PdB_x nanomaterials with different B contents in DMF solution, with $NaBH_4$ serving as both a reductant and a B source (Fig. 3B).[69] In DMF solution, $NaBH_4$ can be dissociated into Na^+ and BH_4^-, due to the relatively strong solvation of Na^+ by DMF molecules.[72] Then, relatively stable BH_4^- in the polar aprotic solvent such as DMF further was used as a reductant and dopant to synthesize PdB_x nanomaterials. The content of B could be tuned by changing the reaction time and $NaBH_4$ concentration. PdB_x with the largest B content (20 at%) showed an apparent peak shift than pure Pd (Fig. 3C). Importantly, with the increase of the B content, the ORR activity of PdB_x was gradually enhanced. Besides PdB_x, $NaBH_4$ could be used to synthesize other noble metal borides. For example, Li *et al.* prepared trace B-doped osmium (Os) (B–Os) aerogel in aqueous solution using $NaBH_4$ as a reductant and a B source.[70] XRD pattern and aberration-corrected HAADF STEM confirmed that the B–Os aerogels showed an enlarged lattice distance than pure hexagonal-close-packed (hcp) Os, attributed to the insertion of B atoms. The resultant B–Os aerogels demonstrated excellent HER catalytic activity in pH-universal electrolytes. The authors claimed that the strong electronic interaction between B and Os atoms could reduce the dissociation energy barrier of H_2O and H absorption energy to promote HER activity. In addition, the B-doped rhodium (Rh) aerogel was also reported *via* one-pot synthesis by applying $NaBH_4$ as the reductant and B source.[73] In addition to the abovementioned one-pot methods, Duan *et al.* reported a two-step method to synthesize B-doped iridium (Ir) nanosheets (IrB NSs) supported on nickel (Ni) foam by using $NaBH_4$ as the B source.[74] Ir NSs on the Ni foam support were first prepared by reducing $IrCl_3$. The Ir NSs/Ni form was then boronized in $NaBH_4$-H_2O solution in an ice bath for 5 h. After B doping, lattice spacing on the $(111)_f$ crystal plane of IrB NSs was 0.225 nm, larger than that of pure Ir (0.218 nm) (Fig. 3D and E). Moreover, the main diffraction peak, $(111)_f$ of IrB NSs

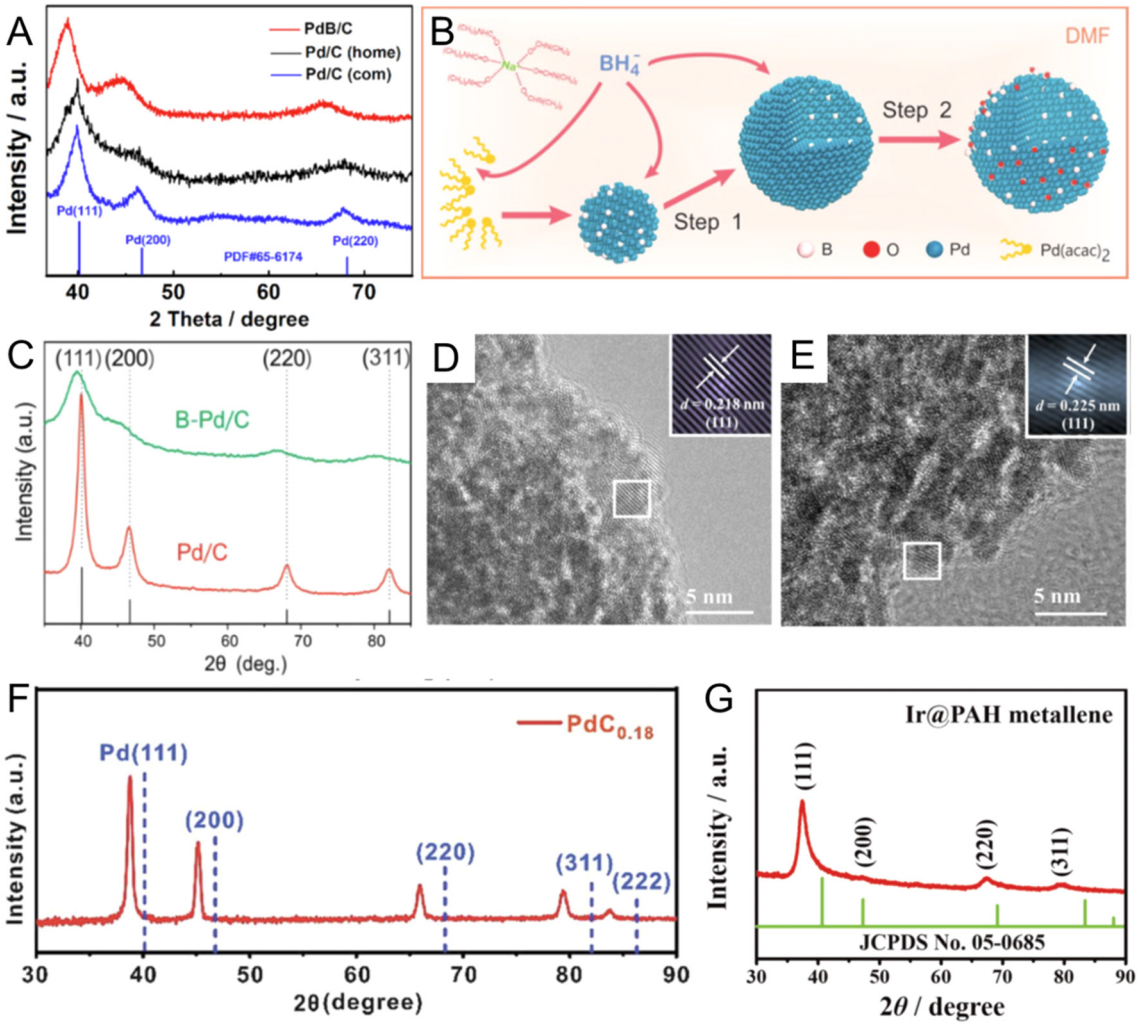

Fig. 3 (A) XRD patterns for PdB/C, commercial and homemade Pd/C. Reproduced with permission from ref 59. Copyright 2018, American Chemical Society. (B) Illustration of the synthesis procedure and formation mechanism of Pd_xB/C. (C) XRD patterns of B-Pd/C and Pd/C. Reproduced with permission from ref 69. Copyright 2017, American Chemical Society. HRTEM images of (D) Ir and (E) IrB nanosheets. Reproduced with permission from ref 74. Copyright 2023, Elsevier. (F) XRD pattern of $PdC_{0.18}$ nanocubes. Reproduced with permission from ref 24 Copyright 2019, Royal Society of Chemistry. (G) XRD pattern of Ir@PAH metallene. Reproduced with permission from ref 86. Copyright 2022, Wiley-VCH.

slightly shifts to a lower angle region compared with that of Ir NSs, indicating the B doping induced expansion of Ir–Ir interplanar spacing. Compared with Ir NSs, IrB NSs showed enhanced performance for the HER and hydrazine oxidation reaction.

Noble metal carbides. As one of the cheapest elements, C has attracted increasing attention for alloying metals to modify their physical, chemical, and mechanical properties.[75–77] For example, inserting trace amounts of C into the iron lattice could make steel harder and stronger. However, only a few efforts in the past were made to develop noble metal carbides, especially by the wet chemical method, likely due to the often-harsh synthesis conditions to obtain noble metal carbides.[78,79] For instance, Guo *et al.* reported a series of fcc PdC_x nanocubes with tunable C/Pd ratios from 0.04 to 0.18 by heating the as-synthesized Pd nanocubes with α-D-glucose in oleylamine under 200 °C for different lengths of time.[24] During heating, C atoms released by α-D-glucose would diffuse into interstitial sites of the Pd lattice. The resultant $PdC_{0.18}$ had a larger lattice fringe of $(200)_f$ plane (0.2 nm) than that of pure Pd (0.19 nm) as suggested by the XRD patterns (Fig. 3F). In the alkyne semihydrogenation reaction, $PdC_{0.18}$ nanocatalysts exhibited higher selectivity (>99%) towards alkenes compared with pure Pd and PdC_x with other stoichiometries, due to the higher desorption rates of alkenes on the $PdC_{0.18}$ surface evidenced by the Fourier transform infrared spectroscopy. Except for Pd, the insertion of C atoms in the gold (Au) lattice can also enhance the catalytic performance in the hydrogenation reaction.[80] Sun *et al.* prepared C-doped Au (C–Au) nanoparticles supported on ordered mesoporous carbon by a hydrothermal method.[80] The authors supposed that the added phenolic resins and triblock copolymer would decompose during

heating to small molecules like CH_4, and these monoatomic C precursors could accelerate the diffusion of the C adatom into the Au surface. The enlarged lattice distance of the Au $(111)_f$ plane was confirmed by aberration-corrected HAADF-STEM images, suggesting the interstitial occupation of C atoms. The C–Au nanocatalyst demonstrated a threefold increase in the turnover frequency (TOF) and superior chemoselectivity (>99%) for 3-vinylaniline in the hydrogenation of 3-nitrostyrene, surpassing the undoped Au/TiO_2 catalyst. Theoretical calculations suggested that interstitial C atoms could reduce the dissociation energy barrier of H_2 and promote the perpendicular adsorption of nitro groups on the C–Au surface, thereby enhancing the selectivity towards 3-vinylaniline.

Noble metal nitrides. Metal nitrides are non-stoichiometric and interstitial nanocompounds with metallic properties.[16,81] N generally tends to incorporate into the interstitial sites in metal lattices with different stoichiometries and endow metals with unique properties like high structural stability under harsh conditions,[82] superior electrical conductivities,[83] and high melting point.[84] However, the synthesis of metal nitrides, especially noble metal nitrides, usually requires extreme conditions like high pressure (above 58 kPa) and high temperature, due to the unreactive N source and high metal–N bond formation energy.[12,85] Thus, there are a few reports of noble metal nitrides synthesized by the wet chemical method. In a recent work, Deng *et al.* reported ultrathin Ir@Poly (allylamine hydrochloride) (PAH) metallene nanosheets with a lateral dimension of about 100 nm by heating the $IrCl_3$, PAH and HCOOH in deionized water at 95 °C for 4 h.[86] Energy dispersive X-ray (EDX) elemental mapping proved that the N element from PAH mainly distributed in the exterior of the Ir@PAH metallene. In addition, the XRD pattern (Fig. 3G) showed that all diffraction peaks of Ir@PAH metallene nanosheets left shifted to a lower degree compared with those of fcc Ir. The lattice expansion in Ir@PAH metallene could be a combined result of N insertion and PAH-induced Ir surface hydroxylation. In EXAFS spectra, extra signals of Ir L_3-edge in Ir@PAH metallene were observed, from which the Ir–N bonding could be derived with a bond length of around 2.13 Å. Compared with Ir nanosheets and commercial Pt/C, Ir@metallene exhibited better electrocatalytic activity and more robust stability for the HER in an acidic medium. The authors suggested that PAH molecules can optimize the electronic structure of Ir metallene due to strong N–Ir interaction and help Ir capture H ions to form proton-rich intermediates, which is favorable for the HER in an acidic environment.

Noble metal phosphides. Different from the above-mentioned light nonmetal elements with small atomic radii (including H, B, C, and N), P has a larger atomic radius and can either occupy the interstitial sites of the host metal lattice or partially substitute host metal atoms.[12,14,87] The replacement/insertion of P into noble metals will affect their electronic structures and therefore physicochemical properties.[14] This section mainly discusses the lattice strain effect on the host metals that originated from P incorporation and its impact on their catalytic performances in chemical reactions.[14,32] For instance, Guo *et al.* developed three kinds of ultrathin Pd phosphide (PdP_x) nanosheets exposed with different low-index facets ($\{100\}_f$, $\{110\}_f$ and$\{111\}_f$) by using different surfactants, employing sodium hypophosphite (NaH_2PO_4) as the P source (Fig. 4A).[88] Fig. 4B–D illustrate the typical TEM and XRD characterization of the PdP_x nanosheet in the case of exposing $\{100\}_f$ facet. According to the XRD results (Fig. 4D), PdP_x nanosheets with a $\{100\}_f$ basal plane exhibited typical fcc diffraction peaks and were left-shifted compared with the standard Pd peaks, indicating that tensile strain was induced after the introduction of P element. PdP_x nanosheets with the $\{110\}_f$ and $\{111\}_f$ basal planes also exhibited similar lattice expansion (Fig. 4A). High-resolution X-ray photoelectron spectroscopy (XPS) showed that there exists charge transfer between Pd and P. Thanks to such reconstruction of electronic configuration by P doping, specific activity of PdP_x nanosheets with $\{100\}_f$ exposed facets was as high as to 172.2 mA cm^{-2} towards the ethanol oxidation reaction (EOR), much higher than that of commercial Pd/C catalysts (30.8 mA cm^{-2}). As an alternative to the inorganic P source, such as NaH_2PO_4, organic compounds may also provide P during the wet chemical synthesis. Guo *et al.* designed a phosphorization treatment to synthesize Pt phosphide (Pt_2P) nanoparticles by treating Pt nanocubes with tri-*n*-octylphosphine (TOP) at 300 °C for 3 hours through a surface atomic diffusion process.[89] The morphology changed from a cubic to spherical shape (Fig. 4E) after the introduction of P. HRTEM image of a single Pt_2P nanoparticle along the $[011]_f$ zone axes demonstrated the interplanar distance of the (111) facet to be 0.27 nm (Fig. 4F), larger than that of metallic Pt (111). In addition, the XRD pattern indicated that the as-prepared Pt_2P possessed the fcc phase with a noticeable peak shift to lower angles due to P insertion (Fig. 4G). In the ORR, the Pt_2P catalyst showed 10.3 times enhanced mass activity compared to the commercial Pt/C catalyst. In addition to the lattice expansion of noble metals caused by P insertion, lattice shrinkage could also be induced by partially replacing noble metal atoms with P. For instance, Mao *et al.* synthesized Rh phosphide (RhP_x) mesoporous nanoparticles by reducing potassium hexachlororhodate(III) (K_2RhCl_6) and sodium hypophosphite (NaH_2PO_2) *via* a wet chemical method. The XRD peak of RhP_x is slightly right-shifted compared with that of Rh nanocrystals, indicating the shrinkage of the lattice in RhP_x ascribed to the doping of P.[90]

2.1.2. Lattice symmetry engineering. In section 2.1.1, we introduced that the incorporation of light nonmetal elements could tune the local lattice distance of the host noble metal and induce strain. In addition to that, introducing light nonmetal elements could also directly alter the host metal lattice symmetry *via* forming a new crystal structure or even a highly disordered amorphous phase (Fig. 1B). As is known, noble metals naturally crystallize in close–packed structures. Specifically, the thermodynamically stable phase of bulk-size Pd, Pt, Ir, Rh, silver (Ag), and Au is fcc while the thermodynamically stable phase of ruthenium (Ru) and Os in bulk is hcp. Many efforts have been made to transform the conventional phases of noble metal nanomaterials into their uncon-

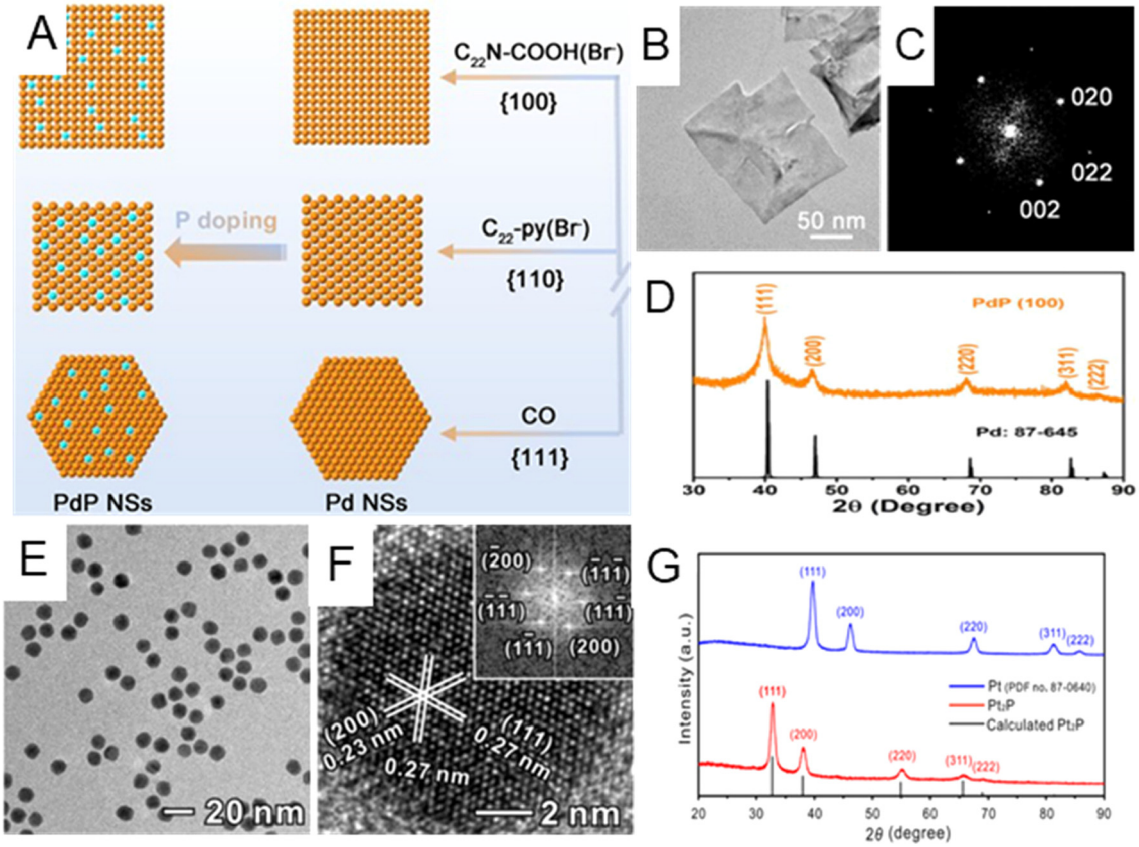

Fig. 4 (A) Schematic illustration of the growth mechanism for three types of PdP_x nanosheets with different exposed PdP_x facets, namely $\{100\}_f$, $\{110\}_f$, and $\{111\}_f$. (B) HRTEM image, (C) the corresponding Fourier diffractogram, and (D) XRD patterns of PdP_x nanosheets with the $\{100\}_f$ facet. Reproduced with permission from ref 88. Copyright 2022, American Chemical Society. (E) Low-magnification TEM image of Pt_2P nanocrystals. (F) HRTEM image of a single Pt_2P nanoparticle. Inset: the corresponding fast Fourier transformation (FFT) pattern. (G) XRD patterns for Pt_2P and Pt. Reproduced with permission from ref 89. Copyright 2019, American Chemical Society.

ventional ones to promote their catalytic properties.[18,19,91,92] The insertion of light nonmetal elements provides a strategy to achieve the phase (or lattice symmetry) transformation of noble metal nanomaterials *via* forming noble metal-based nanocompounds. In this section, some representative works about wet chemical lattice symmetry engineering of noble metal-based nanomaterials will be discussed. Note that for noble metal hydride nanomaterials, no wet chemical method has been reported to date, except one interesting report that observed H-induced fcc-to-hcp transformation of Pd nanocrystals in a liquid cell TEM.[93] The following paragraphs in this section focus on other types of noble metal-based nanomaterials.

Noble metal borides. In section 2.1.1, we summarized the recent works to prepare fcc PdB_x nanomaterials by the wet chemical method. However, previous attempts could only achieve low B contents (<20 at%) and maintain the fcc Pd lattice.[67,69] Density functional theory (DFT) calculations showed that on further increasing the B content in the PdB_x compound, the hcp Pd_2B phase could become thermodynamically stable.[94] In 2017, Kobayashi *et al.* successfully prepared the first hcp Pd_2B nanocrystals by inserting higher content of B atoms (~35 at%) into as-synthesized fcc Pd nanocubes in BH_3–THF solution below 80 °C for 6 days (Fig. 5A).[68] The novel hcp structure of Pd_2B was confirmed by the synchrotron powder XRD and aberration-corrected HAADF-STEM, where the Pd atoms showed characteristic hcp packing sequence of ABAB along the diagonal direction (Fig. 5B and C). In addition, electron-energy loss spectroscopy (EELS) demonstrated the homogeneous distribution of B atoms in the Pd lattice. Different from the synthesis method reported by Kobayashi *et al.*,[68] Chen *et al.* used DMAB as the B source to synthesize hcp Pd_2B nanosheets *via* heating DMAB and fcc Pd nanosheets in DMF solution at 120 °C with a shorter time (only 2 h).[95] The authors further used DFT calculations to study the mechanism of B insertion into the Pd lattice and proposed that the insertion of B was accompanied by a layer-by-layer transition of the Pd lattice symmetry from fcc to hcp. Moreover, compared with fcc Pd, fcc PdB_x and fcc/hcp PdB_x, Pd_2B with a pure hcp structure showed the best HER performance, due to the decreased formation energy of H_2 caused by the formation of the hcp phase. In the above two cases, B atoms are randomly distributed in the Pd lattice. Lv *et al.* reported hcp Pd_2B mesoporous nanocrystals with ordered sequences of Pd/B atoms (hcp-mesoPd_2B-o) using DMAB as

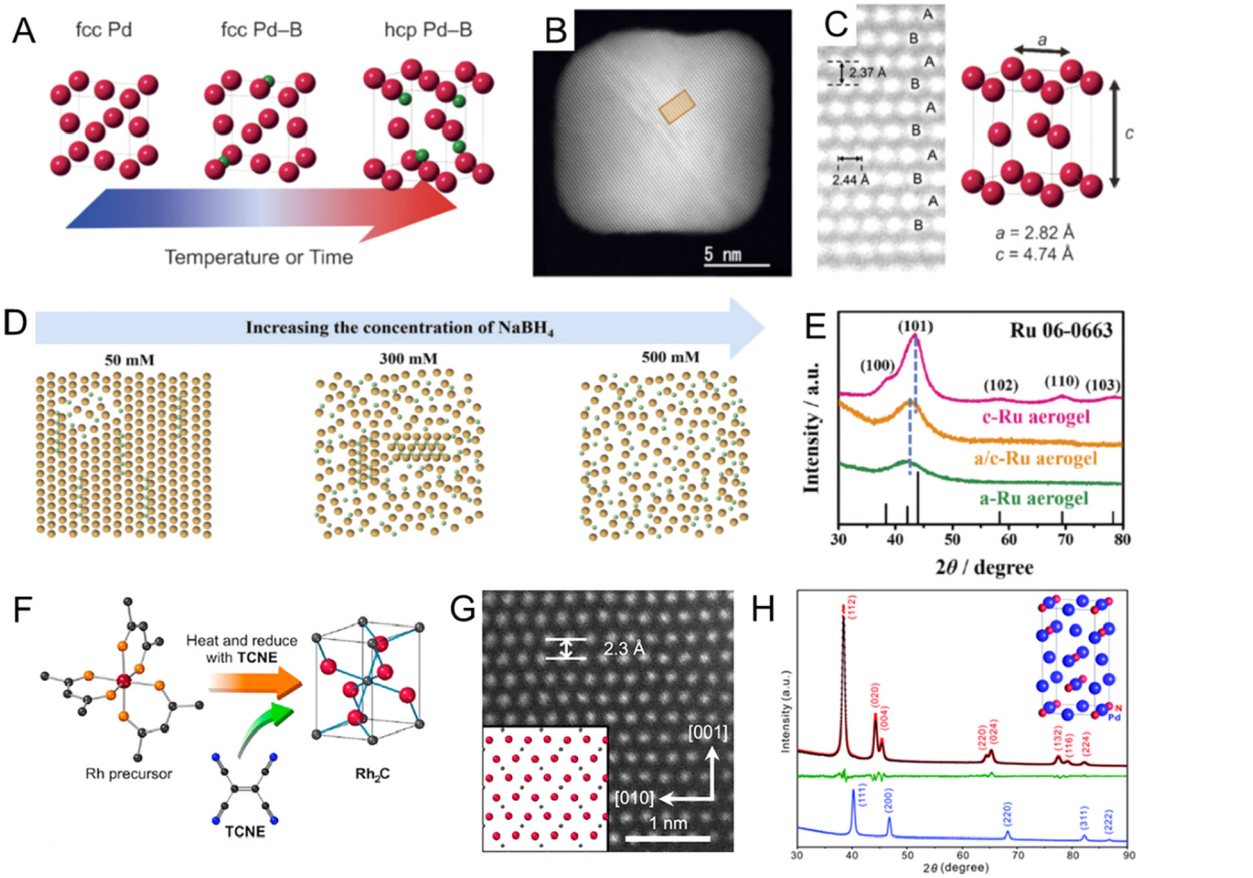

Fig. 5 (A) Schematic illustration of structure rearrangement of Pd NCs induced by heavy B doping. (B) Aberration-corrected high-angle annular dark-field scanning transmission electron microscopy (HAADF-STEM) image of hcp Pd_2B nanocrystal and (C) magnified image of the rectangular region in (B). The bright dots correspond to Pd atoms. Reproduced with permission from ref 68. Copyright 2017, Wiley-VCH. (D) Schematic diagram of the atoms of the RuB aerogel when the concentration of the B source, was increased from 50 to 500 mM. (E) XRD patterns for a/c-RuB, a-RuB and c-RuB aerogels. Reproduced with permission from ref 97. Copyright 2023, Wiley-VCH. (F) Illustration of the synthesis of Rh_2C nanocrystal. TCNE: tetracyanoethylene. (G) Aberration-corrected HAADF-STEM image of the Rh_2C nanocrystal along the [100] zone axis. Reproduced with permission from ref 99. Copyright 2020, American Chemical Society. (H) XRD patterns of Pd nanocubes (blue line), Pd_2N nanocrystals (black line), and Rietveld refinement of Pd_2N nanocrystals. The red and green lines showed the calculated curve and the difference plot, respectively. Reproduced with permission from ref 106. Copyright 2021, Royal Society of Chemistry.

the B source.[96] By gradually increasing the reaction temperature, lattice evolution from fcc mesoPd to fcc-mesoPd_5B (100 °C), hcp-mesoPd_2B-r (140 °C) with randomly distributed B, and finally hcp-mesoPd_2B-o (160 °C) with atomically ordered B was achieved. The hcp-mesoPd_2B-o showed faster full conversion (~80s) to the reduction of p-nitrophenol than fcc-mesoPd_5B (~105s) and Pd black (~235s).

Doping with B could also lead to the lattice distortion of the noble metal to eventually form amorphous structures.[71,97] For example, amorphous RhB and amorphous/fcc heterophase RhB metallene were synthesized by mixing the crystalline fcc Rh metallene with $NaBH_4$ dissolved in DMF solution in an ice bath.[71] The crystallinity of RhB metallene could be tuned by the length of the boronization time, resulting in the formation of amorphous/fcc heterophase RhB (8 h) and amorphous RhB (16 h). No lattice fringe, diffusion ring, or diffraction peak could be observed in HRTEM, selected area diffraction (SAED) or XRD results, respectively, confirming the absence of crystalline structures in RhB. Due to the abundant phase boundaries in amorphous/fcc heterophase RhB metallene, it showed improved activity toward both the HER and H_2O_2 electrooxidation reaction as compared to crystalline fcc Rh metallene and amorphous RhB metallene. Recently, the same research group developed a general method to synthesize a series of amorphous/crystalline heterophase metal boride aerogels (RuB, PtB, PdB, and RhB) by reducing metal precursors with $NaBH_4$.[98] In particular, the crystallinity of the RuB aerogel could be controlled by the concentration of $NaBH_4$ (Fig. 5D). When the concentration of $NaBH_4$ was as high as 500 mM, an amorphous RuB aerogel could be obtained (Fig. 5E). The HER activity of the amorphous/crystalline heterophase RuB aerogel under alkaline conditions was superior to Pt/C, amorphous RuB, and crystalline RuB, owing to the most abundant catalytic sites in the amorphous/crystalline heterophase structure.

Noble metal carbides. C could form various carbides with non-noble metals and change their lattice symmetry, such as

tungsten carbide (WC),[75] iron carbide (Fe_3C),[76] and cobalt carbide (Co_2C).[77,98] However, noble metal carbides have not been observed in bulk size.[99] As for noble metal carbides, although PdC_x[24] and AuC_x[80] nanocrystals have been synthesized as introduced in section 2.1.1, the lattice symmetry of Pd and Au in the noble metal carbides still maintained the fcc phase, probably due to the low C content. Recent studies showed that it is possible to change the lattice symmetry of noble metals in noble metal carbides when the C content increases, which showed enhanced catalytic performance than their parent metal counterparts.[99,100] For example, Wakisaka *et al.* reported a novel rhodium carbide (Rh_2C) nanocrystal with an orthorhombic phase by a liquid-phase synthesis (Fig. 5F).[99] Naturally, the lattice symmetry of Rh is highly symmetric fcc. Interestingly, due to the existence of interstitial C in the Rh lattice, the Rh atoms in Rh_2C had a hcp-like packing sequence and showed ABAB packing sequence along the [001] zone axis (Fig. 5G). The authors proposed that the organic oxidant, tetracyanoethylene, served as a C source and gradually decomposed to release C atoms during heating. fcc Rh nanocrystals were obtained without adding tetracyanoethylene. Synchrotron PXRD and NPD were performed to confirm the position of C atoms and the ratio of Rh to C. Both patterns fitted well with the hypothetical patterns of Rh_2C with the orthorhombic phase. Moreover, the orthorhombic phase Rh_2C nanocatalysts demonstrated higher HER performance than their fcc Rh counterpart in alkaline solution due to the unique packing sequence of Rh and the alloying effect of C. In another recent work, Cao *et al.* developed another strategy to synthesize orthorhombic phase RhC_x nanomaterials *via* reducing the Rh precursor in a mixture of formaldehyde and oleylamine under 200 °C.[100] The Rh lattice symmetry was transformed from fcc to an orthorhombic structure when half of the lattice octahedral sites were occupied by C atoms, which was confirmed by NPD. The existence of C atoms was further confirmed by low-frequency Raman spectral characterization. Interestingly, the same approach was further extended to insert C atoms into commercial fcc Rh black, leading to partial transformation into the orthorhombic RhC_x phase. Compared with its fcc Rh counterpart, the RhC_x nanocatalysts exhibited enhanced selectivity and activity toward the electrocatalytic EOR. The authors supposed that electronic and geometric effects induced by C insertion could decrease the energy barrier of the dehydrogenation step in the EOR and suppress side reactions, resulting in enhancement in both activity and selectivity.

Noble metal nitrides. Previous studies have shown that lattice symmetry engineering of metal nitrides could be achieved by the CVD method, in which the metal nitrides were prepared *via* the reaction between metal/metal precursors and ammonia gas (NH_3),[101–103] as well as using the magnetron sputtering method.[104] In comparison, wet chemical synthesis was less reported. In 2011, Wu *et al.* successfully prepared the first transition metal nitride, *i.e.*, cubic Cu_3N nanocrystals by a wet chemical technique.[105] However, there are limited reports on the synthesis of noble metal nitrides with novel crystal structures by the wet chemical method due to the inert nature of both the noble metal and the N–N triple bond. Recently, Guo *et al.* reported a facile hydrothermal method to synthesize a series of PdN_x nanocubes with controllable stoichiometries ($PdN_{0.08}$, $PdN_{0.18}$, $PdN_{0.26}$, $PdN_{0.35}$, and Pd_2N) by heating urea, PVP and pre-prepared Pd nanocubes in deionized water at 180 °C for 1 h.[106] During heating, the decomposition of urea could release N atoms, which further diffused into the Pd lattice. Interestingly, on inserting more N atoms into the Pd lattice and reaching an N/Pd ratio of 0.5, the fcc Pd nanocubes transformed into tetragonal phase Pd_2N nanocubes (Fig. 5H). In XPS, an extra peak of N 1s can be observed at 397.3 eV in the spectra for Pd_2N nanocubes, indicating the presence of the Pd–N interaction. The enlarged lattice fringes of (100) (2.04 Å) for Pd_2N measured b HRTEM also confirmed that N atoms diffused into the Pd lattice. Compared with undoped Pd/C and fcc PdN_x with other stoichiometries, the tetragonal Pd_2N exhibited much higher activity for the ORR under alkaline conditions. The authors believed that catalytic activity for the ORR in an alkaline medium were enhanced with an increasing N/Pd ratio in PdN_x nanocatalysts. The introduction of N atoms into Pd lattices could downshift the d-band center of Pd and weaken the binding interaction between the Pd surface and the adsorbates. The excellent catalytic performance could also be attributed to the unique polycrystalline structure of tetragonal Pd_2N. Cao *et al.* reported an AgN_3-catalyzed hydroazidation reaction of terminal alkynes in which AgN_3 was converted from Ag_2CO_3 during the reaction and simultaneously proved to be a robust catalyst.[107] The authors supposed that Ag_2CO_3 was quickly and completely converted to AgN_3 during the hydroazidation reaction of *p*-tolylacetylene. The fast conversion of Ag_2CO_3 to AgN_3 took place within 5 min, as reflected by the pure orthorhombic AgN_3 diffraction peaks in the XRD pattern. This work provided a novel and facile preparation strategy for the design and preparation of noble metal-based catalysts for organic reactions.

Noble metal phosphides. When alloying nonmetal elements with larger atomic radii, such as P, it is easier to change the original crystal symmetry of the host noble metal by forming metal phosphide compounds.[16] Different lattice symmetries and varying P contents can modify physicochemical properties of noble metal phosphides.[13] To date, many types of noble metal phosphides, including RhP_x,[108–111] RuP_x,[21,112,113] PdP_x,[114,115–117] and Au_2P_3,[118] have been synthesized by the wet chemical method. For example, Wang *et al.* fabricated wrinkled Rh_2P nanosheets by heating as-prepared fcc Rh nanosheets in tri-*n*-octylphosphine solution.[108] The phosphating reaction occurred through the thermal decomposition of tri-*n*-octylphosphine. The wrinkled morphology of the Rh_2P nanosheets and the elemental mapping of Rh and P was confirmed by TEM and EDX (Fig. 6A). The ratio of Rh to P was estimated to be ~2 : 1 (Fig. 6B). The XRD pattern of the sample matched well with that of cubic phase Rh_2P (Fig. 6B). According to the XPS spectrum of Rh 2d, Rh in Rh_2P showed a slightly positive valence state. The wrinkled Rh_2P nanosheets exhibited better HER activity with an overpotential of 18.3 mV

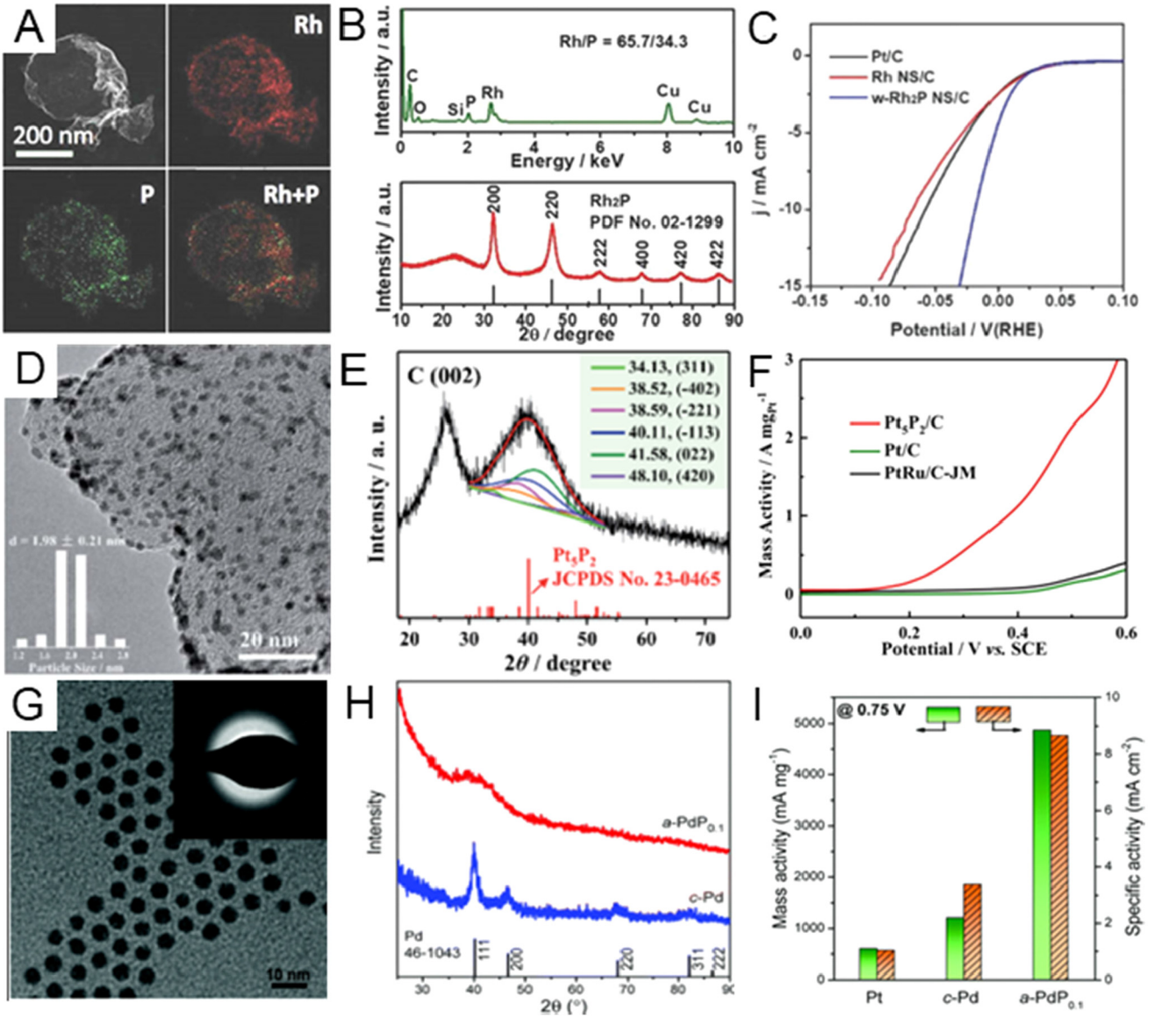

Fig. 6 (A) HAADF-STEM image of wrinkled Rh_2P nanosheets and energy dispersive X-ray (EDX) elemental mappings of Rh and P. (B) XRD pattern and EDX spectrum of Rh_2P nanosheets. (C) The comparison of active current density of wrinkled Rh_2P, Rh nanosheets and Pt/C for the hydrogen evolution reaction (HER) in 0.1M KOH solution. Reproduced with permission from ref 108. Copyright 2018, Wiley-VCH. (D) TEM image and (E) XRD pattern of the Pt_5P_2/C catalyst. (F) The comparison of mass activity of Pt_5P_2/C, commercial Pt/C, and PtRu/C catalysts for the methanol oxidation reaction (MOR) in 0.5 M H_2SO_4 solution containing 1.0 M CH_3OH. Reproduced with permission from ref 119. Copyright 2020, Royal Society of Chemistry. (G) TEM image of amorphous PdP alloy nanoparticles (a-$PdP_{0.1}$). Inset: the corresponding selected area electron diffraction (SAED) patterns showing no obvious diffraction spots. (H) XRD patterns of a-$PdP_{0.1}$ and crystalline Pd nanoparticles (c-Pd). (I) Comparison of electrochemical performances of a-$PdP_{0.1}$ and c-Pd in the ethanol oxidation reaction. Reproduced with permission from ref 125. Copyright 2022, Royal Society of Chemistry.

at a current density of 10 mA cm^{-2}, much lower than commercial Pt/C (58.4 mV) and Rh nanosheets/C (68.9 mV) (Fig. 6C). In addition to the HER, noble metal phosphides have also been highly catalytically active toward the MOR. Li *et al.* developed a strategy to synthesize monodisperse Pt_5P_2 nanoparticles (Fig. 6D), which could serve as a MOR electrochemical catalyst.[119] In the synthesis process of Pt_5P_2 nanoparticles, a mixed aqueous dispersion of carbon black, sodium hypophosphite, and dibasic sodium phosphate (P sources) was first prepared, followed by adding chloroplatinic acid hexahydrate ($H_2PtCl_6{\cdot}6H_2O$) as the Pt sources. The final product was obtained after heat treatment at 125 °C under reflux for 4 h. The diffraction peaks of pre-obtained Pt_5P_2 nanoparticles were indexed into the monoclinic phase of the Pt_5P_2 nanocrystal, and the fcc Pt characteristic peaks could not be observed in the XRD pattern, confirming the full phosphorization of Pt (Fig. 6E). In the MOR test, the mass activity of Pt_5P_2 (3.60 A mg_{Pt}^{-1}) was found to be 11.0 and 9.1 times better than those

of commercial Pt/C (0.33 A mg_{Pt}^{-1}) and PtRu/C (0.39 A mg_{Pt}^{-1}) (Fig. 6F), which indicated that the MOR kinetics may be accelerated on the Pt_5P_2 surface. Besides, the introduction of P atoms can also lead to lattice distortion of the original metal lattice to form amorphous materials, which are promising catalyst materials due to their abundant random directional bonds, surface unsaturated atoms, and abundant defects.[120–122] One possible mechanism for the formation of amorphous noble metal phosphides is the simultaneous diffusion of the P element into the interstitial and substitutional positions of host metal lattice, destroying the previous long-range order of the crystal structure.[14,123,124] Zhang *et al.* successfully prepared amorphous PdP (a-Pd) nanoparticles with enhanced EOR performance in comparison with crystalline Pd nanoparticles (c-Pd).[125] The well-dispersed a-Pd nanoparticles (Fig. 6G) were synthesized by the reduction of the Pd salt in the mixture solution of TOP and oleylamine. The XRD pattern of a-PdP confirmed the amorphous structure, while clear diffraction peaks were observed in the XRD pattern of c-Pd nanoparticles (Fig. 6H). As for the EOR performance, a-PdP showed high reactivity of 4851 mA mg^{-1} at 0.75 V, which was higher than those of c-Pd and commercial Pt/C catalysts in Fig. 6I. The discovery of this process has important guiding significance for precious metal phosphorization, promoting nano-structural diversification.

Noble metal sulfides. Similar to P, incorporating S into noble metals can also significantly alter the crystal lattice of the host metal *via* the formation of noble metal sulfides. Theoretical studies have shown that electron transfer between d orbitals of precious metals and p orbitals of S can greatly adjust the electrocatalytic performance of noble metal sulfide catalysts.[12,14,32,87] Motivated by such an advantage, numerous endeavors have been dedicated to the controlled synthesis of noble metal sulfide nanomaterials.[126–133] Among the synthetic methods of noble metal sulfides, one-step synthesis is the most direct and efficient way. For instance, Du *et al.* synthesized monodisperse palladium sulfide (Pd_4S) nanoparticles through a simple one-pot method.[130] To be specific, the as-synthesized Pd_4S was obtained by heating $Pd(acac)_2$ and S powder in oleylamine at 320 °C *via* a one-pot sulfurization process. Monodisperse Pd_4S nanoparticles had a uniform size distribution of about 10 nm (Fig. 7A), and the lattice spacing of Pd_4S nanoparticles are 0.21 and 0.36 nm (Fig. 7B), which matched well with the (211) and (110) planes of the tetragonal Pd_4S nanocrystal. In the alkaline solution, the as-obtained Pd_4S/C catalyst exhibits good ORR performance, better than commercial Pt/C illustrated in Fig. 7C. In addition to the one-pot method to obtain noble metal sulfides, researchers also developed multi-step wet chemical methods, including template-assisted[134,135] and cation displacement methods.[135–137]

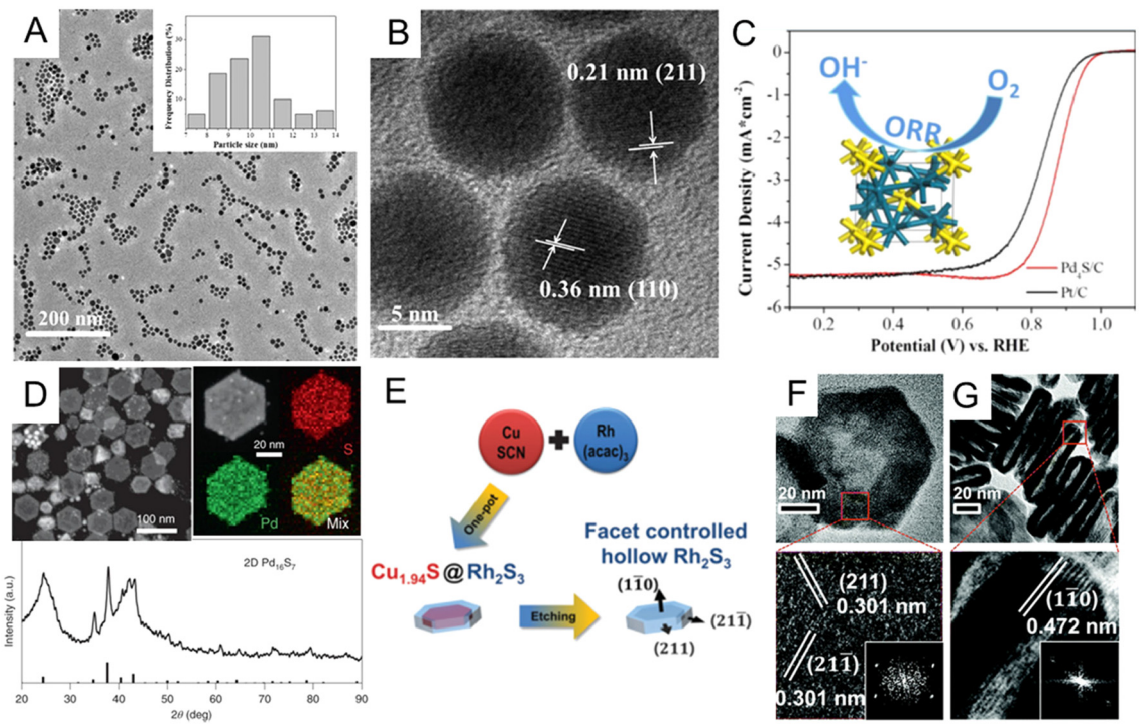

Fig. 7 (A) Low-magnification TEM and (B) HRTEM images of Pd_4S nanoparticles. (C) Comparison of oxygen reduction reaction (ORR) performances of the Pd_4S/C and commercial Pt/C catalysts. Reproduced with permission from ref 130. Copyright 2018, American Chemical Society. (D) HAADF-STEM image, EDX element mappings, and X-ray diffraction pattern of $Pd_{16}S_7$ nanosheets prepared by cation exchange from the Cu_xS_y template. Reproduced with permission from ref 135. Copyright 2022, Nature Publishing Groups. (E) Schematic illustration of the formation of hollow Rh_2S_3 catalysts. TEM and HRTEM images of the (F) top-view and (G) side-view of Rh_2S_3 hollow structures. Inset: corresponding FFT patterns. Reproduced with permission from ref 136. Copyright 2016, Royal Society of Chemistry.

Here, we only discuss a few representative reports. Park *et al.* have illustrated the synthesis of core@crown $Cu_{1.81}S@IrS_2$ hexagonal nanoplates *via* a template-assisted method.[137] To prepare this core@crown structure, pre-obtained $Cu_{1.8}S$ nanoplates were dispersed in oleylamine, followed by adding iridium acetylacetonate and heat treatment at 240 °C for 0.5 h. As triclinic $Cu_{1.81}S$ and orthorhombic IrS_2 have similar sulfur sublattices, epitaxial interfaces may be formed with IrS_2 crowns at the $Cu_{1.81}S$ surfaces. In one systematic experimental study of the cation exchange method, Feng *et al.* developed a general synthesis strategy to prepare a library of noble metal chalcogenides using Cu chalcogenides as a sacrificial template for subsequent cation displacement.[135] For example, two-dimensional $Pd_{16}S_7$ nanosheets were synthesized by cation exchange from Cu_xS_y with the presence of ethylene glycol. The complete transformation of Cu_xS_y into $Pd_{16}S_7$ was confirmed by XRD patterns and element mappings (Fig. 7D). Since both template synthesis and cation exchange can effectively control the shape and crystal facet, more efforts have been made to combine these methods for more diversified noble metal sulfide nanostructures. For example, Yoon *et al.* reported hollow rhodium sulphide (Rh_2S_3) nano-prisms as a HER catalyst with excellent catalytic activity and long-term durability.[136] As shown in Fig. 7E, the hollow Rh_2S_3 nanoplate was obtained by etching $Cu_{1.94}S@Rh_2S_3$ core–shell structures, which were first prepared by one-pot heating of copper(I) thiocyanate and $Rh(acac)_3$ mixture. The whole process was believed to combine cation exchange, galvanic replacement, and the Kirkendall effect. The hexagonal faces of the orthorhombic Rh_2S_3 nanoprisms were assigned to {110} facets (Fig. 7F and G), and it was found that the six sides of hexagonal nanoprisms are {211} facets through HRTEM and FFT images. The Rh_2S_3 catalyst exhibited excellent stability after 10 000 cycles under strongly acidic conditions. This combination of multiple synthetic strategies greatly expanded the variety of complex sulfide nanostructures that could be designed and fabricated, providing novel electrochemical catalysts for advanced catalysis such as carbon dioxide electroreduction (CO_2RR).

In addition, S doping into the noble metal could also cause heavy lattice distortion that may inevitably induce the reconstruction of the original electron configuration and generate a disordered lattice. For example, Xu *et al.* devised a way to prepare amorphous RuS_2 (a-RuS_2) nanoparticles dispersed on carbon spheres *via* a one-pot solvothermal method.[138] To be specific, the a-RuS_2 nanoparticles could be formed by the reduction of ruthenium(III) chloride trihydrate and L-cysteine (as the S source) in the aqueous dispersion of hollow carbon spheres at 160 °C for 9 h. The prepared a-RuS_2 nanoparticles with a diameter of 2.6 nm were distributed uniformly on the carbon framework, which were beneficial for exposing more active sites and improving atomic utilization, enhancing the electrocatalytic HER. In addition to the direct one-pot method, amorphous noble metal sulfides can also be obtained by sulfurization progress in multiple steps. For instance, Xie *et al.* prepared amorphous S-doped Pd metallenes *via* a two-step solvothermal method.[139] The Pd metallenes were first prepared and re-dispersed in oleylamine containing S powder under heat treatment at 210 °C for 1 h. After sulfurizing Pd metallene, the amorphous structure could be obtained, as no lattice fringes or diffraction peaks were observed in HRTEM images and XRD results, respectively. In the MOR, the amorphous S–Pd metallene catalyst showed better reaction activity compared with commercial Pd/C and Pt/C catalysts.

2.2. Indirect lattice engineering of noble metal–light nonmetal nanocompounds

Besides directly inserting foreign elements, we can also utilize a coherent metal–metal interface and engineer the lattice strain indirectly. For example, building core–shell structures has been proven as an effective strategy to tune the lattice strain of shell metals, which could be induced by the lattice mismatch between the core and the shell.[20,140,141] Specifically, the exposed facets, surface morphology, and composition of the core metals can be utilized to modify the strain level in shell metals.[142–144] Recently, by inserting or extracting light nonmetal elements into or from the core metal in a core–shell nanostructure, fine lattice strain engineering of different noble metals has been proven to be possible.[145] For instance, a seed-mediated growth method was applied to synthesize PdH_x@Ru metallenes *via* reducing $RuCl_3{\cdot}xH_2O$ in the formaldehyde solution with Pd metallenes as the seed.[146] In the reaction process, while the H atoms were generated by the decomposition of formaldehyde and inserted into the lattice of Pd metallenes to form PdH_x, Ru(III) was reduced to Ru(0) on the surface of PdH_x to form atomically thin Ru layers (Fig. 8A). The average Pd–Pd/Ru bond length was estimated by FFT-extended EXAFS spectra of the Pd K-edge (Fig. 8B) to be 2.55 Å, which was 0.1 Å longer than that in Pd foil, indicating that lattice expansion in the Pd core came from inserting H atoms. The expanded lattice of PdH_x relative to Pd resulted in a 4.5% tensile strained Ru skin. The formation of tensile strained Ru skin in PdH_x@Ru was proven by the Ru–Ru/Pd bond length, which was 0.11 Å longer than that of Ru foil (Fig. 8C). The authors claimed that the tensile strained Ru skin enabled higher catalytic activity and better stability in the HER, which was evidenced by spectroscopic analyses and DFT calculations. In addition to the Ru skin, Pt skin in cubic and octahedral $PdH_{0.43}$@Pt core–shell nanoparticles with exposed $(200)_f$ and $(111)_f$ facets, respectively, were synthesized *via* Pd-seeded epitaxial growth followed by the introduction of H into Pd to form $PdH_{0.43}$.[26] The enlarged lattice fringes of the Pt $(200)_f$ plane (2.01 Å, red rectangle in Fig. 8D and F) in cubic-$PdH_{0.43}$@Pt NPs (c-$PdH_{0.43}$@Pt NPs) measured from aberration-corrected STEM were larger than that of the $(200)_f$ plane (1.93 Å) in c-Pd@Pt NPs, and the octahedral-$PdH_{0.43}$@Pt NPs (o-$PdH_{0.43}$@Pt) had a larger Pt $(111)_f$ plane (2.45 Å, red rectangle in Fig. 8E and G) than that of the Pt $(111)_f$ plane (2.37 Å) in o-Pd@Pt NPs. These measurements proved that the Pt shells were stretched, likely

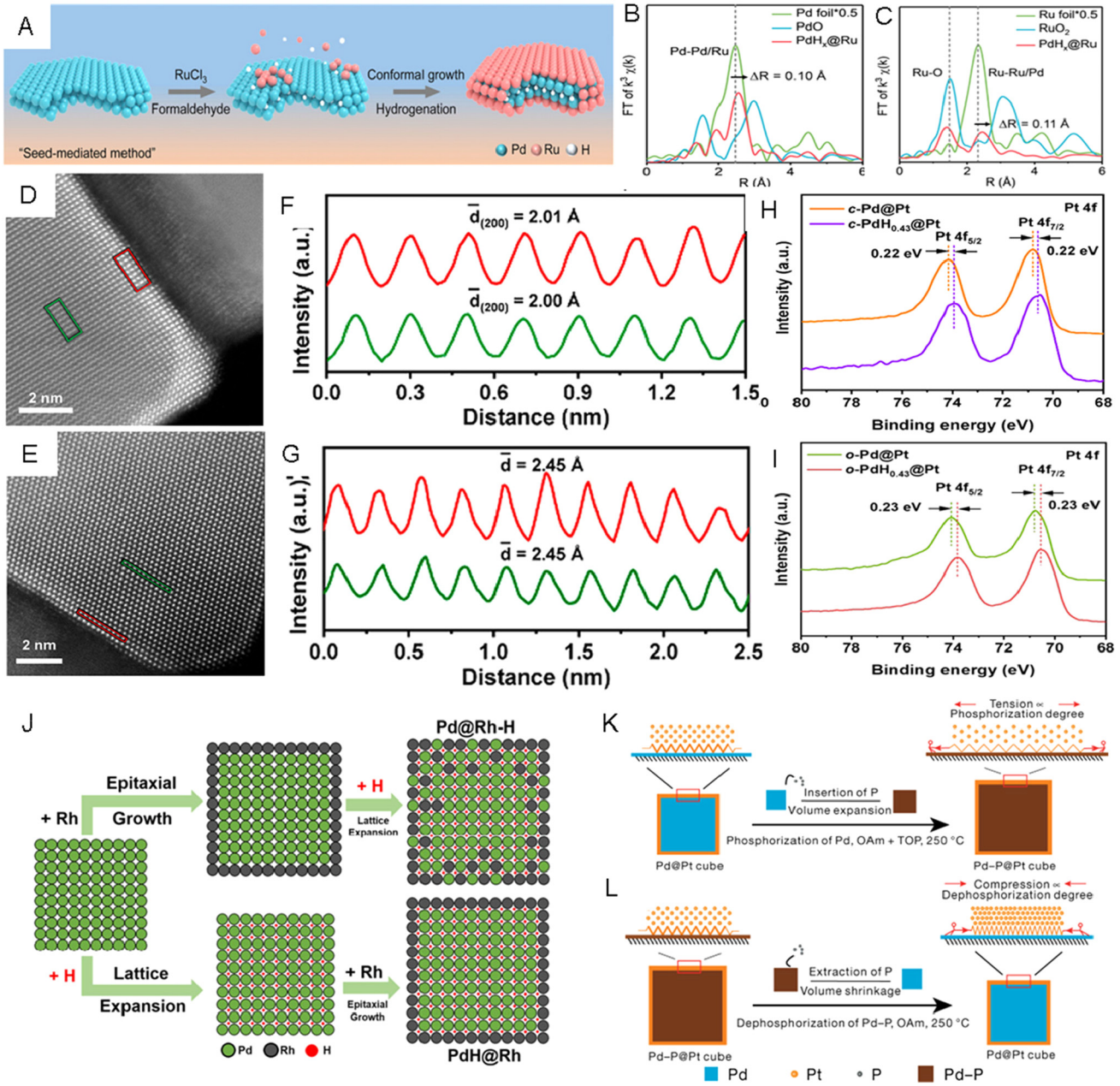

Fig. 8 (A) Schematic illustration of the preparation of PdH_x@Ru metallenes. (B and C) FFT-extended X-ray absorption fine structure (EXAFS) spectra of (B) Pd K-edge and (C) Ru K-edge in Ru foil, RuO_2, and PdH_x@Ru metallenes. Reproduced with permission from ref 146. Copyright 2023, American Chemical Society. (D) Aberration-corrected HAADF-STEM images taken from the (D) c-$PdH_{0.43}$@Pt nanocubes and (E) o-$PdH_{0.43}$@Pt nanooctahedra. (F and G) Integrated pixel intensities of the $PdH_{0.43}$ core and Pt shell taken from the green and red rectangular regions in D and G, respectively. (H and I) X-ray photoelectron spectroscopy (XPS) spectra of Pt 4f in (H) c-Pd@Pt and c-$PdH_{0.43}$@Pt nanocubes, as well as (I) in o-Pd@Pt and o-$PdH_{0.43}$@Pt nanooctahedra. Reproduced with permission from ref 26. Copyright 2021, American Chemical Society. (J) Schematic illustration of the formation of Pd@Rh–H and PdH@Rh nanocubes with two different H insertion pathways. Reproduced with permission from ref 148. Copyright 2021, springer. (K and L) Schematic illustrations of (K) the tensile strain formation on the Pt shell by inserting P in Pd nanocubes and (L) compression strain formation on the Pt shell by extracting P from Pd-P nanocubes. Reproduced with permission from ref 25. Copyright 2021, Nature Publishing Groups.

caused by the lattice expansion of the Pd core during hydrogenation. In the XPS spectra of Pt 4f, the binding energies of c-$PdH_{0.43}$@Pt NPs reduced by about 0.22 eV compared to that of c-Pd@Pt NPs (Fig. 8H) and the o-$PdH_{0.43}$@Pt NPs exhibited lower binding energies (around 0.23 eV) compared to that of o-Pd@Pt NPs (Fig. 8I) both resulting from the successful insertion of H atoms into Pd shells. Compared with c-Pd@Pt and o-Pd@Pt, both c-$PdH_{0.43}$@Pt and o-$PdH_{0.43}$@Pt NPs exhibited higher catalytic activities in the MOR. Recently, few-layer Ir skins with different tensile strains were prepared using lattice

engineered Pd-based octahedral nanocrystals with different H contents, namely o-Pd@Ir-1.2%, o-Pd@Ir-1.7% and o-Pd@Ir-2.1%.[147] The XRD pattern showed that the peaks of o-Pd@Ir-1.2% matched well with those of the standard Pd pattern, while all the diffraction peaks of o-Pd@Ir-1.7% and o-Pd@Ir-2.1% left shifted to lower angles, confirming the presence of lattice expansion in the latter two samples. In the XPS spectrum of Ir 4f, the peak shifted to higher binding energy region with increasing tensile strain in Ir shells from 1.2% to 2.1%, indicating the gradually decreased electron density at the Ir shell with expanding lattices. The authors reported a volcano-shaped correlation between the strain of the Ir shell and its catalytic performances in the HER. The o-Pd/lr-1.7% NPs exhibited the highest mass activity and the lowest overpotential relative to other two catalysts. Based on theoretical analysis, the medium tensile strain on the Ir $(111)_f$ surface was believed to lower the adsorption strength of H intermediates. Interestingly, switching the sequence of epitaxial growth of the shell metal and doping of interstitial H in the core metal may yield different core–shell hydrides. Guo *et al.* reported the synthesis of Pd@Rh–H nanocubes by first epitaxial growth of Rh shells on Pd nanocubes and then H insertion, and in another experiment, $PdH_{0.43}$@Rh nanocubes by first inserting H on Pd nanocubes followed by epitaxial growth of Rh.[148] As shown in the scheme (Fig. 8J), to prepare Pd@Rh–H core–shell nanocubes, Pd seeds were first epitaxially coated with Rh to form Pd@Rh core–shell nanocubes, which were then treated by a H doping process, forming a Rh-doped PdH core and Pd-doped Rh shell along with lattice expansion. In another route to prepare $PdH_{0.43}$@Rh core–shell nanocubes, epitaxial growth of

Table 1 Summary of representative reports on lattice strain engineering of noble metal-based nanocatalysts *via* incorporating light nonmetal elements

Name of noble metal nanocompound	Wet chemical method	Types of lattice strain	Catalytic application	Ref
PdH_x nanocrystals	Solvothermal	Tensile strain	—	51
$PdH_{0.43}$ nanopolycrystals	Solvothermal	Tensile strain	MOR	23
$PdH_{0.43}$ nanotetrahedra;	Solvothermal	Tensile strain	MOR	23
$PdH_{0.43}$ nanocubes	Hydrothermal + solvothermal	Tensile strain	MOR	23
PdH_x nanodendrites	Solvothermal	Tensile strain	FAOR; HER	52
PdH_x/C (x = 0.10, 0.29, 0.23, 0.43)	Solvothermal	Tensile strain	FAOR	53
PdH_x nanooctahedra;	Hydrothermal + solvothermal	Tensile strain	FAOR	55
PdH_x nanoicosahedra	Solvothermal	Tensile strain	FAOR	55
RhH nanosheet	Solvothermal	Tensile strain	HER	44
PdB_x/C	Hydrothermal	Tensile strain	FAOR	58
PdB_x/C	Hydrothermal	Tensile strain	Formic acid deposition reaction	59
PtB_x/C	Solvothermal	Tensile strain	ORR	60
PdB_x/C	Solvothermal	Tensile strain	Hydrogenation of 3-hexyn-1-ol	67
PdB_x nanoparticles	Solvothermal	Tensile strain	ORR	69
OsB_x aerogels	Hydrothermal	Tensile strain	HER	70
RhB_x aerogels	Hydrothermal	Tensile strain	HER	73
IrB_x nanosheets supported on Ni foam	Hydrothermal + solvothermal	Tensile strain	Hydrazine oxidation reaction; HER;	74
$PdC_{0.18}$ nanocubes	Hydrothermal + solvothermal	Tensile strain	Alkyne semihydrogenation reaction	24
AuC_x nanoparticles	Hydrothermal	Tensile strain	Hydrogenation of 3−nitrostyrene	80
Ir@PAH metallene	Hydrothermal	Tensile strain	HER	86
PdP_x nanosheets	Hydrothermal	Tensile strain	EOR	88
Pt_2P nanoparticles	Hydrothermal + solvothermal	Tensile strain	ORR	89
RhP_x nanoparticles	Hydrothermal + solvothermal	Compressive strain	HER	90
PdH_x@Ru core–shell metallenes	Hydrothermal + solvothermal + epitaxial growth	Tensile strain	HER	146
$PdH_{0.43}$@Pt core–shell nanocubes	Hydrothermal + solvothermal + epitaxial growth	Tensile strain	MOR	26
$PdH_{0.43}$@Pt core–shell nanooctahedra	Hydrothermal + solvothermal + epitaxial growth	Tensile strain	MOR	26
PdH_x@Ir core–shell nanoparticles	Solvothermal + epitaxial growth	Tensile strain	HER	147
Pd@Rh–H core–shell nanocubes	Hydrothermal + solvothermal + epitaxial growth	Tensile strain	MOR	148
$PdH_{0.43}$@Rh core–shell nanocubes	Hydrothermal + solvothermal + epitaxial growth	Tensile strain	MOR	148
PdP_x@Pt core–shell nanocubes	Hydrothermal + solvothermal + epitaxial growth	Tensile strain	HER; MOR	25
PdP_x@Pt-derived Pd@Pt core–shell nanocubes	Hydrothermal + solvothermal + non-epitaxial growth	Compressive strain	HER; MOR	25

MOR: methanol oxidation reaction; FAOR: formic acid oxidation reaction; HER: hydrogen evolution reaction; ORR: oxygen reduction reaction; and EOR: ethanol oxidation reaction.

Table 2 Summary of representative reports on lattice symmetry engineering of noble metal-based nanocatalysts *via* incorporating light nonmetal elements

Name of noble metal nanocompound	Wet chemical method	Type of lattice symmetry	Catalytic application	Ref
Pd_2B nanocubes	Hydrothermal + solvothermal	hcp	—	68
Pd_2B nanosheets	Solvothermal	hcp	HER	95
Pd_2B mesoporous nanocrystals	Hydrothermal + solvothermal	hcp	P-Nitrophenol reduction reaction	96
RhB metallenes	Hydrothermal + solvothermal	Amorphous + amorphous/fcc heterophase	HER; hydrogen peroxide electrooxidation reaction	71
RuB aerogels	Hydrothermal	Amorphous/hcp heterophase	HER	97
Rh_2C nanocrystals	Solvothermal	Orthorhombic	HER	99
RhC_x	Solvothermal	Orthorhombic	EOR	100
Pd_2N nanocubes	Hydrothermal	Tetragonal	ORR	106
AgN_3	Solvothermal	Orthorhombic	Hydroazidation reaction of *p*-tolylacetylene	107
Rh_2P nanosheets	Solvothermal	Cubic	HER	108
Pt_5P_2 nanoparticles	Hydrothermal	Monoclinic	MOR	119
PdP nanoparticles	Solvothermal	Amorphous	EOR	125
Pd_4S nanoparticles	Solvothermal	Tetragonal	ORR	130
IrS_2 shells	Solvothermal + epitaxial growth	Orthorhombic	N/A	137
Rh_2S_3 nanoprisms	Solvothermal + acidic etching	Orthorhombic	HER	136
RuS_2 nanoparticles	Solvothermal	Amorphous	HER	138
PdS_x metallenes	Solvothermal	Amorphous	ORR	139

hcp: hexagonal-close-packed; fcc: face-centered cubic; MOR: methanol oxidation reaction; FAOR: formic acid oxidation reaction; HER: hydrogen evolution reaction; ORR: oxygen reduction reaction; and EOR: ethanol oxidation reaction.

Rh was achieved after transforming the Pd core into $PdH_{0.43}$ nanocompounds (Fig. 8J). It is worth mentioning that the XPS peaks of Pd 3d in Pd@Rh–H showed lower binding energy than $PdH_{0.43}$@Rh, suggesting that the intermixing of the less electronegative Rh with PdH may promote the electron transfer from Rh to Pd. The more effective charge transfer and formation of mixed alloy hydride on the surface of Pd@Rh–H made it a more active and stable MOR catalyst as compared to $PdH_{0.43}$@Rh (Table 1).

Different from the above work, He *et al.* achieved both tensile strain and compression strain on Pt shells by inserting P into Pd@Pt core–shell nanocubes and extracting P from PdP_x@Pt core–shell nanocubes, repectively.[25] The authors claimed that P could diffuse into the Pd lattice of Pd@Pt core–shell nanocubes to form PdP_x@Pt, while keeping Pt undoped. Therefore, the tensile strain in the Pt shells could be created due to the increased volume of the PdP_x cores (Fig. 8K). With the increase of the phosphorization time, both the volume of the PdP_x core and the tensile strain in Pt skin gradually increased with the increased P contents. On the other hand, compressive strain control was achieved by dephosphorizing PdP_x@Pt nanocubes with different P contents *via* heat treatment. The Pd cores derived from PdP_x would shrink after the dephosphorization process, causing compression strain in Pt $(100)_f$ shells (Fig. 8L). The lattice tensions and compressions in Pt $(100)_f$ were tailored from −5.1% to +5.9%. The authors supposed that both tensile and compressive strain could enhance the catalytic activity and provide excellent durability toward the MOR, but excessive strain could diminish the catalytic performance (Table 2).[149]

3. Conclusion

In this mini-review, we present the recent development of lattice engineering in noble metal–light nonmetal binary nanocompounds together with some of their derived core–shell nanomaterials. *Via* wet chemical methods, lattice engineering of noble metal-based nanomaterials has been realized *via* either directly inserting light nonmetal elements into the metal lattice or indirectly tuning an epitaxial metal–metal compound interface. Their lattice variation in terms of strain and symmetry could be well characterized thanks to various advanced characterization technologies. Importantly, alloying noble metals with Earth-abundant light nonmetal elements has not only decreased the usage of noble metals in catalysts, but also improved their intrinsic catalytic performance by modifying their electronic states. With the great potential, there are still many challenges and opportunities in this direction.

Firstly, although the wet chemical method has been successfully exploited to incorporate a light nonmetal with noble metal nanomaterials in some studies, there are still limitations of current approaches. (1) The diversity of wet chemically prepared noble metal–light nonmetal compounds is very limited compared to those prepared by other methods such as the gas–solid method and vapor transport method. There are especially limited methods to prepare C- and N-doped noble metal nanomaterials,[150] probably because they are thermodynamically less favorable.[151] Therefore, further development of feasible wet-chemical approaches to synthesize and stabilize a wider library of noble metal–light nonmetal compounds is

desired. (2) Precisely controlled lattice engineering of the nanostructures, including morphology,[152,153] composition,[154] and crystal structure, remains a challenge. At most wet chemical synthesis temperatures, the light elements are often randomly distributed and unstable in noble metal lattices, which also highly depends on the type of precursors, solvents, temperature, and other synthetic parameters. Overall, the current understanding of the formation and stabilization mechanism of various noble metal compounds is preliminary and identifying the critical synthesis conditions remains important.

Secondly, although inserting light nonmetal elements into noble metal lattices provides an effective way to transform the lattice symmetry of host metals, it is still a great challenge to prepare noble metal nanomaterials with controlled unconventional phases. Recent studies show that phase engineering of nanomaterials plays an important role in tuning the physicochemical properties of noble metal nanomaterials.[18,91,155] Inspired by this concept, indirect approaches by using noble metal nanocompounds with various crystal phases as the phase template to epitaxially grow shell metals with unconventional phases beome a promising solution. For example, orthorhombic phase Rh_2C nanocompounds might be applied as the template to epitaxially grow noble metal shells or even non-noble metal shells with the unconventional orthorhombic phase by wet chemical epitaxial growth. In such way, a variety of heterostructured nanomaterials with unconventional phases could be precisely designed to further study their phase-dependent catalytic properties for enhanced performances.

Thirdly, the concept of inserting guest elements with smaller size to tune the lattice structures of host materials can also be extended to engineer the lattice of more kinds of nanomaterials, such as metal–organic frameworks, covalent organic frameworks, and high-entropy alloys. For example, small molecules could be inserted into the pores of metal–organic frameworks to cause lattice distortion and meanwhile modify their functions. In another recent study, N element could be inserted into Pt-based high-entropy alloy nanoparticles to cause tensile strain, resulting in improved ORR activity and durability.[156] These examples show great potential for extending the lattice engineering concepts in this review to a broader range of nanomaterials.

Lastly, although superior catalytic performances have been reported in the HER, ORR, and MOR, deeper insights into the relationship between the electrochemical performance and lattice structure of noble metal compounds are still required. It is therefore important to study in-depth factors that affect the performance of the catalytic system by combining advanced characterization strategies with theoretical calculations, aiming for rational design and reliable explanation. Additionally, there are a number of burgeoning electrochemical reactions that may unlock more potential of noble metal compounds for various applications, such as the nitrogen reduction reaction (NRR), nitrate reduction reaction (NO_3RR) and CO_2RR. For example, Pd-based nanocompounds are intensively studied for fuel cell applications,[116] but there are few research reports on their applications in other reactions such as the CO_2RR, in which metallic Pd-based nanocatalysts have been proven to be promising.[157] Besides electrocatalytic applications, more efforts could be made to explore other important categories of catalytic reactions, such as thermal catalysis and photocatalysis, to expand the potential applications of lattice-engineered noble metal compounds.

Conflicts of interest

There are no conflicts to declare.

Acknowledgements

Y.C. thanks the support from Start-up Fund (Project No. 4930977) and the Direct Grant for Research (Project No. 4053444) from the Chinese University of Hong Kong.

References

1 M. Li, Z. Zhao, T. Cheng, A. Fortunelli, C.-Y. Chen, R. Yu, Q. Zhang, L. Gu, B. V. Merinov and Z. Lin, *Science*, 2016, **354**, 1414–1419.
2 Q. Guan, C. Zhu, Y. Lin, E. I. Vovk, X. Zhou, Y. Yang, H. Yu, L. Cao, H. Wang, X. Zhang, X. Liu, M. Zhang, S. Wei, W.-X. Li and J. Lu, *Nat. Catal.*, 2021, **4**, 840–849.
3 M. Zhao, Z. Chen, Y. Shi, Z. D. Hood, Z. Lyu, M. Xie, M. Chi and Y. Xia, *J. Am. Chem. Soc.*, 2021, **143**, 6293–6302.
4 X. Ren, X. Dong, L. Liu, J. Hao, H. Zhu, A. Liu and G. Wu, *SusMat*, 2023, **3**, 442–470.
5 Z. W. Seh, J. Kibsgaard, C. F. Dickens, I. Chorkendorff, J. K. Nørskov and T. F. Jaramillo, *Science*, 2017, **355**, eaad4998.
6 F. Meemken and A. Baiker, *Chem. Rev.*, 2017, **117**, 11522–11569.
7 J. Xie, Y. Jiang, S. Li, P. Xu, Q. Zheng, X. Fan, H. Peng and Z. Tang, *Acta Phys.-Chim. Sin*, 2023, **39**, 2306037.
8 S. Guo and E. Wang, *Nano Today*, 2011, **6**, 240–264.
9 L. Zhang, Q. Chang, H. Chen and M. Shao, *Nano Energy*, 2016, **29**, 198–219.
10 X.-F. Yang, A. Wang, B. Qiao, J. Li, J. Liu and T. Zhang, *Acc. Chem. Res.*, 2013, **46**, 1740–1748.
11 Y. Xia, Y. Xiong, B. Lim and S. E. Skrabalak, *Angew. Chem., Int. Ed.*, 2009, **48**, 60–103.
12 H. Chen, B. Zhang, X. Liang and X. Zou, *Chin. J. Catal.*, 2022, **43**, 611–635.
13 J. Liu, C. Lee, Y. Hu, Z. Liang, R. Ji, X. Y. D. Soo, Q. Zhu and Q. Yan, *SmartMat*, 2023, **4**, e1210.
14 C. Zhang, W. Liu, C. Chen, P. Ni, B. Wang, Y. Jiang and Y. Lu, *Nanoscale*, 2022, **14**, 2915–2942.
15 H.-l. Liu, F. Nosheen and X. Wang, *Chem. Soc. Rev.*, 2015, **44**, 3056–3078.

16 R. Guo, K. Zhang, S. Ji, Y. Zheng and M. Jin, *Chin. Chem. Lett.*, 2021, **32**, 2679–2692.
17 T. Chen, C. Foo and S. C. E. Tsang, *Chem. Sci.*, 2021, **12**, 517–532.
18 Y. Chen, Z. Lai, X. Zhang, Z. Fan, Q. He, C. Tan and H. Zhang, *Nat. Rev. Chem.*, 2020, **4**, 243–256.
19 H. Li, X. Zhou, W. Zhai, S. Lu, J. Liang, Z. He, H. Long, T. Xiong, H. Sun, Q. He, Z. Fan and H. Zhang, *Adv. Energy Mater.*, 2020, **10**, 2002019.
20 X. Yang, Y. Wang, X. Tong and N. Yang, *Adv. Energy Mater.*, 2022, **12**, 2102261.
21 Z. Pu, I. S. Amiinu, Z. Kou, W. Li and S. Mu, *Angew. Chem., Int. Ed.*, 2017, **56**, 11559–11564.
22 X. Ai, X. Zou, H. Chen, Y. Su, X. Feng, Q. Li, Y. Liu, Y. Zhang and X. Zou, *Angew. Chem., Int. Ed.*, 2020, **59**, 3961–3965.
23 Z. Zhao, X. Huang, M. Li, G. Wang, C. Lee, E. Zhu, X. Duan and Y. Huang, *J. Am. Chem. Soc.*, 2015, **137**, 15672–15675.
24 R. Guo, Q. Chen, X. Li, Y. Liu, C. Wang, W. Bi, C. Zhao, Y. Guo and M. Jin, *J. Mater. Chem. A*, 2019, **7**, 4714–4720.
25 T. He, W. Wang, F. Shi, X. Yang, X. Li, J. Wu, Y. Yin and M. Jin, *Nature*, 2021, **598**, 76–81.
26 G. Liu, W. Zhou, Y. Ji, B. Chen, G. Fu, Q. Yun, S. Chen, Y. Lin, P.-F. Yin, X. Cui, J. Liu, F. Meng, Q. Zhang, L. Song, L. Gu and H. Zhang, *J. Am. Chem. Soc.*, 2021, **143**, 11262–11270.
27 V. J. Parks and A. J. Durelli, *Exp. Mech.*, 1967, **7**, 279–280.
28 H. Wang, S. Xu, C. Tsai, Y. Li, C. Liu, J. Zhao, Y. Liu, H. Yuan, F. Abild-Pedersen and F. B. Prinz, *Science*, 2016, **354**, 1031–1036.
29 L. Nguyen, H.-P. Komsa, E. Khestanova, R. J. Kashtiban, J. J. Peters, S. Lawlor, A. M. Sanchez, J. Sloan, R. V. Gorbachev and I. V. Grigorieva, *ACS Nano*, 2017, **11**, 2894–2904.
30 M. Escudero-Escribano, P. Malacrida, M. H. Hansen, U. G. Vej-Hansen, A. Velázquez-Palenzuela, V. Tripkovic, J. Schiøtz, J. Rossmeisl, I. E. Stephens and I. Chorkendorff, *Science*, 2016, **352**, 73–76.
31 Z. Xi, X. Cheng, Z. Gao, M. Wang, T. Cai, M. Muzzio, E. Davidson, O. Chen, Y. Jung and S. Sun, *Nano Lett.*, 2019, **20**, 272–277.
32 Z. Li, X. Lu, J. Teng, Y. Zhou and W. Zhuang, *Nanoscale*, 2021, **13**, 11314–11324.
33 J. Norton and J. Sowa, *Chem. Rev.*, 2016, **116**, 8315–8317.
34 S. Kato, S. K. Matam, P. Kerger, L. Bernard, C. Battaglia, D. Vogel, M. Rohwerder and A. Züttel, *Angew. Chem., Int. Ed.*, 2016, **55**, 6028–6032.
35 T. Zhang, H. Miyaoka, H. Miyaoka, T. Ichikawa and Y. Kojima, *ACS Appl. Energy Mater.*, 2018, **1**, 232–242.
36 J. Fan, X. Cui, S. Yu, L. Gu, Q. Zhang, F. Meng, Z. Peng, L. Ma, J.-Y. Ma, K. Qi, Q. Bao and W. Zheng, *ACS Nano*, 2019, **13**, 12987–12995.
37 Y. Xiong, Y. Ma, L. Zou, S. Han, H. Chen, S. Wang, M. Gu, Y. Shen, L. Zhang, Z. Xia, J. Li and H. Yang, *J. Catal.*, 2020, **382**, 247–255.
38 Y. Shi, R. Schimmenti, S. Zhu, K. Venkatraman, R. Chen, M. Chi, M. Shao, M. Mavrikakis and Y. Xia, *J. Am. Chem. Soc.*, 2022, **144**, 2556–2568.
39 M. K. Kabiraz, J. Kim, W.-J. Lee, B. Ruqia, H. C. Kim, S.-U. Lee, J.-R. Kim, S.-M. Paek, J. W. Hong and S.-I. Choi, *Chem. Mater.*, 2019, **31**, 5663–5673.
40 X. Guo, Z. Hu, J. Lv, J. Qu and S. Hu, *Dalton Trans.*, 2021, **50**, 10359–10364.
41 J. Wu, X. Cui, J. Fan, J. Zhao, Q. Zhang, G. Jia, Q. Wu, D. Zhang, C. Hou, S. Xu, D. Jiao, L. Gu, D. J. Singh and W. Zheng, *ACS Energy Lett.*, 2021, **6**, 1912–1919.
42 C. Zhan, H. Li, X. Li, Y. Jiang and Z. Xie, *Sci. China Mater.*, 2020, **63**, 375–382.
43 Y. Zhu, C. Gao, S. Bai, S. Chen, R. Long, L. Song, Z. Li and Y. Xiong, *Nano Res.*, 2017, **10**, 3396–3406.
44 J. Fan, Y. Zhang, W. Liu, M. Li, Y. Cai, Q. Ji, Z. Zhao, G. Hou, A. Li, W. Zhou, L. Yu and D. Deng, *Matter*, 2023, **6**, 3877–3888.
45 G. Wang, J. Liu, Y. Sui, M. Wang, L. Qiao, F. Du and B. Zou, *J. Mater. Chem. A*, 2019, **7**, 14876–14881.
46 R. Lässer and K. H. Klatt, *Phys. Rev. B: Condens. Matter Mater. Phys.*, 1983, **28**, 748–758.
47 F. D. Manchester, A. San-Martin and J. M. Pitre, *J. Phase Equilib.*, 1994, **15**, 62–83.
48 J. E. Schirber and B. Morosin, *Phys. Rev. B: Solid State*, 1975, **12**, 117–118.
49 J. E. Worsham, M. K. Wilkinson and C. G. Shull, *J. Phys. Chem. Solids*, 1957, **3**, 303–310.
50 J. A. Eastman, L. J. Thompson and B. J. Kestel, *Phys. Rev. B: Condens. Matter Mater. Phys.*, 1993, **48**, 84–92.
51 T.-H. Phan and R. E. Schaak, *Chem. Commun.*, 2009, 3026–3028, DOI: **10.1039/B902024A**.
52 H.-Y. Sun, Y. Ding, Y.-Q. Yue, Q. Xue, F.-M. Li, J.-X. Jiang, P. Chen and Y. Chen, *ACS Appl. Mater. Interfaces*, 2021, **13**, 13149–13157.
53 J. Zhang, M. Chen, H. Li, Y. Li, J. Ye, Z. Cao, M. Fang, Q. Kuang, J. Zheng and Z. Xie, *Nano Energy*, 2018, **44**, 127–134.
54 Y. Wang, S. N. Sun and M. Y. Chou, *Phys. Rev. B: Condens. Matter Mater. Phys.*, 1996, **53**, 1–4.
55 S. Zhou, M. Figueras-Valls, Y. Shi, Y. Ding, M. Mavrikakis and Y. Xia, *Angew. Chem., Int. Ed.*, 2023, **62**, e2023069.
56 H. Li, X. Qin, X.-G. Zhang, K. Jiang and W.-B. Cai, *ACS Catal.*, 2022, **12**, 12750–12764.
57 M. Fan, X. Liang, Q. Li, L. Cui, X. He and X. Zou, *Chin. Chem. Lett.*, 2023, **34**, 107275.
58 J.-Y. Wang, Y.-Y. Kang, H. Yang and W.-B. Cai, *J. Phys. Chem. C*, 2009, **113**, 8366–8372.
59 B. Jiang, X.-G. Zhang, K. Jiang, D.-Y. Wu and W.-B. Cai, *J. Am. Chem. Soc.*, 2018, **140**, 2880–2889.
60 Z. Mao, C. Ding, X. Liu, Q. Zhang, X. Qin, H. Li, F. Yang, Q. Li, X.-G. Zhang, J. Zhang and W.-B. Cai, *ACS Catal.*, 2022, **12**, 8848–8856.
61 S. S. Djokić, in *Modern aspects of electrochemistry*, Springer, 2002, pp. 51–133.

62 M. Wang, X. Qin, K. Jiang, Y. Dong, M. Shao and W.-B. Cai, *J. Phys. Chem. C*, 2017, **121**, 3416–3423.
63 K. Jiang, J. Chang, H. Wang, S. Brimaud, W. Xing, R. J. Behm and W.-B. Cai, *ACS Appl. Mater. Interfaces*, 2016, **8**, 7133–7138.
64 S. Hong, S. Chung, J. Park, J. P. Hwang, C. H. Lee, S. Uhm, S. Bong and J. Lee, *ACS Catal.*, 2021, **11**, 4722–4729.
65 H. Lv, L. Sun, D. Xu, J. Henzie, Y. Yamauchi and B. Liu, *J. Mater. Chem. A*, 2019, **7**, 24877–24883.
66 Y. Wang, H. Lv, L. Sun, X. Guo, D. Xu and B. Liu, *ACS Appl. Mater. Interfaces*, 2021, **13**, 17599–17607.
67 C. W. A. Chan, A. H. Mahadi, M. M.-J. Li, E. C. Corbos, C. Tang, G. Jones, W. C. H. Kuo, J. Cookson, C. M. Brown, P. T. Bishop and S. C. E. Tsang, *Nat. Commun.*, 2014, **5**, 5787.
68 K. Kobayashi, H. Kobayashi, M. Maesato, M. Hayashi, T. Yamamoto, S. Yoshioka, S. Matsumura, T. Sugiyama, S. Kawaguchi, Y. Kubota, H. Nakanishi and H. Kitagawa, *Angew. Chem., Int. Ed.*, 2017, **56**, 6578–6582.
69 J. Li, J. Chen, Q. Wang, W.-B. Cai and S. Chen, *Chem. Mater.*, 2017, **29**, 10060–10067.
70 Y. Li, C.-K. Peng, H. Hu, S.-Y. Chen, J.-H. Choi, Y.-G. Lin and J.-M. Lee, *Nat. Commun.*, 2022, **13**, 1143.
71 K. Deng, W. Wang, Q. Mao, H. Yu, Z. Wang, Y. Xu, X. Li, H. Wang and L. Wang, *Small*, 2022, **18**, 2203020.
72 F. A. Carey and R. J. Sundberg, Advanced organic chemistry: part A: structure and mechanisms, Springer Science & Business Media, 2007.
73 K. Deng, T. Ren, Y. Xu, S. Liu, Z. Dai, Z. Wang, X. Li, L. Wang and H. Wang, *J. Mater. Chem. A*, 2020, **8**, 5595–5600.
74 Z. Duan, T. Ren, Y. Xu, Z. Wang, H. Yu, K. Deng, L. Wang and H. Wang, *Int. J. Hydrogen Energy*, 2023, **48**, 37045–37052.
75 L. H. Bennett, J. R. Cuthill, A. J. McAlister, N. E. Erickson and R. E. Watson, *Science*, 1974, **184**, 563–565.
76 Y. Hu, J. O. Jensen, W. Zhang, L. N. Cleemann, W. Xing, N. J. Bjerrum and Q. Li, *Angew. Chem., Int. Ed.*, 2014, **53**, 3675–3679.
77 L. Zhong, F. Yu, Y. An, Y. Zhao, Y. Sun, Z. Li, T. Lin, Y. Lin, X. Qi, Y. Dai, L. Gu, J. Hu, S. Jin, Q. Shen and H. Wang, *Nature*, 2016, **538**, 84–87.
78 J. Cored, A. García-Ortiz, S. Iborra, M. J. Climent, L. Liu, C.-H. Chuang, T.-S. Chan, C. Escudero, P. Concepción and A. Corma, *J. Am. Chem. Soc.*, 2019, **141**, 19304–19311.
79 J. Kim, H. J. Kim, B. Ruqia, M. J. Kim, Y.-J. Jang, T. H. Jo, H. Baik, H.-S. Oh, H.-S. Chung, K. Baek, S. Noh, M. Jung, K.-j. Kim, H.-K. Lim, Y.-S. Youn and S.-I. Choi, *Adv. Mater.*, 2021, **33**, 2105248.
80 Y. Sun, Y. Cao, L. Wang, X. Mu, Q. Zhao, R. Si, X. Zhu, S. Chen, B. Zhang, D. Chen and Y. Wan, *Nat. Commun.*, 2020, **11**, 4600.
81 H. Wang, J. Li, K. Li, Y. Lin, J. Chen, L. Gao, V. Nicolosi, X. Xiao and J.-M. Lee, *Chem. Soc. Rev.*, 2021, **50**, 1354–1390.
82 S. Tan, B. M. Tackett, Q. He, J. H. Lee, J. G. Chen and S. S. Wong, *Nano Res.*, 2020, **13**, 1434–1443.
83 B. Avasarala, T. Murray, W. Li and P. Haldar, *J. Mater. Chem.*, 2009, **19**, 1803–1805.
84 P. D. D. Singh, Z. V. P. Murthy and S. K. Kailasa, *Coord. Chem. Rev.*, 2023, **481**, 215046.
85 J. C. Crowhurst, A. F. Goncharov, B. Sadigh, J. M. Zaug, D. Aberg, Y. Meng and V. B. Prakapenka, *J. Mater. Res.*, 2008, **23**, 1–5.
86 K. Deng, T. Zhou, Q. Mao, S. Wang, Z. Wang, Y. Xu, X. Li, H. Wang and L. Wang, *Adv. Mater.*, 2022, **34**, 2110680.
87 T. Chen, C. Foo and S. C. E. Tsang, *Chem. Sci.*, 2021, **12**, 517–532.
88 K. Guo, Y. Meng, R. Guo, H. Guo, S. Qiu, D. Fan, D. Xu and Y. Li, *ACS Appl. Energy Mater.*, 2022, **5**, 10758–10766.
89 R. Guo, W. Bi, K. Zhang, Y. Liu, C. Wang, Y. Zheng and M. Jin, *Chem. Mater.*, 2019, **31**, 8205–8211.
90 Q. Mao, S. Jiao, K. Ren, S. Wang, Y. Xu, Z. Wang, X. Li, L. Wang and H. Wang, *Chem. Eng. J.*, 2021, **426**, 131227.
91 Q. Yun, Y. Ge, Z. Shi, J. Liu, X. Wang, A. Zhang, B. Huang, Y. Yao, Q. Luo, L. Zhai, J. Ge, Y. Peng, C. Gong, M. Zhao, Y. Qin, C. Ma, G. Wang, Q. Wa, X. Zhou, Z. Li, S. Li, W. Zhai, H. Yang, Y. Ren, Y. Wang, L. Li, X. Ruan, Y. Wu, B. Chen, Q. Lu, Z. Lai, Q. He, X. Huang, Y. Chen and H. Zhang, *Chem. Rev.*, 2023, **123**, 13489–13692.
92 Y. Zhai, P. Han, Q. Yun, Y. Ge, X. Zhang, Y. Chen and H. Zhang, *eScience*, 2022, **2**, 467–485.
93 J. Hong, J.-H. Bae, H. Jo, H.-Y. Park, S. Lee, S. J. Hong, H. Chun, M. K. Cho, J. Kim, J. Kim, Y. Son, H. Jin, J.-Y. Suh, S.-C. Kim, H.-K. Roh, K. H. Lee, H.-S. Kim, K. Y. Chung, C. W. Yoon, K. Lee, S. H. Kim, J.-P. Ahn, H. Baik, G. H. Kim, B. Han, S. Jin, T. Hyeon, J. Park, C. Y. Son, Y. Yang, Y.-S. Lee, S. J. Yoo and D. W. Chun, *Nature*, 2022, **603**, 631–636.
94 G.-F. Wei, L.-R. Zhang and Z.-P. Liu, *Phys. Chem. Chem. Phys.*, 2018, **20**, 27752–27757.
95 L. Chen, L.-R. Zhang, L.-Y. Yao, Y.-H. Fang, L. He, G.-F. Wei and Z.-P. Liu, *Energy Environ. Sci.*, 2019, **12**, 3099–3105.
96 H. Lv, D. Xu, C. Kong, Z. Liang, H. Zheng, Z. Huang and B. Liu, *ACS Cent. Sci.*, 2020, **6**, 2347–2353.
97 K. Deng, W. Wang, Z. Lian, H. Yu, Z. Wang, Y. Xu, H. Wang and L. Wang, *Small*, 2023, **19**, 2304181.
98 F. Yu, T. Lin, Y. An, K. Gong, X. Wang, Y. Sun and L. Zhong, *Chem. Commun.*, 2022, **58**, 9712–9727.
99 T. Wakisaka, K. Kusada, D. Wu, T. Yamamoto, T. Toriyama, S. Matsumura, H. Akiba, O. Yamamuro, K. Ikeda, T. Otomo, N. Palina, Y. Chen, L. S. R. Kumara, C. Song, O. Sakata, W. Xie, M. Koyama, Y. Kubota, S. Kawaguchi, R. L. Arevalo, S. M. Aspera, E. F. Arguelles, H. Nakanishi and H. Kitagawa, *J. Am. Chem. Soc.*, 2020, **142**, 1247–1253.
100 Z. Cao, H. Li, Q. Fan, Z. Liu, Z. Chen, Y. Sun, J. Ye, M. Cao, C. Shen, Y. Jiang, M. Chi, J. Cheng, H. Chen, Z. Xie and Y. Xia, *Nano Energy*, 2023, **113**, 108597.

101 K. Xu, P. Chen, X. Li, Y. Tong, H. Ding, X. Wu, W. Chu, Z. Peng, C. Wu and Y. Xie, *J. Am. Chem. Soc.*, 2015, **137**, 4119–4125.
102 B. Cao, G. M. Veith, J. C. Neuefeind, R. R. Adzic and P. G. Khalifah, *J. Am. Chem. Soc.*, 2013, **135**, 19186–19192.
103 J. Xie, S. Li, X. Zhang, J. Zhang, R. Wang, H. Zhang, B. Pan and Y. Xie, *Chem. Sci.*, 2014, **5**, 4615–4620.
104 G. M. Veith, A. R. Lupini, L. Baggetto, J. F. Browning, J. K. Keum, A. Villa, L. Prati, A. B. Papandrew, G. A. Goenaga, D. R. Mullins, S. E. Bullock and N. J. Dudney, *Chem. Mater.*, 2013, **25**, 4936–4945.
105 H. Wu and W. Chen, *J. Am. Chem. Soc.*, 2011, **133**, 15236–15239.
106 R. Guo, K. Zhang, Y. Liu, Y. He, C. Wu and M. Jin, *J. Mater. Chem. A*, 2021, **9**, 6196–6204.
107 S. Cao, Q. Ji, H. Li, M. Pang, H. Yuan, J. Zhang and X. Bi, *J. Am. Chem. Soc.*, 2020, **142**, 7083–7091.
108 K. Wang, B. Huang, F. Lin, F. Lv, M. Luo, P. Zhou, Q. Liu, W. Zhang, C. Yang and Y. Tang, *Adv. Energy Mater.*, 2018, **8**, 1801891.
109 S. Yang, X. Yang, Q. Wang, X. Cui, H. Zou, X. Tong and N. Yang, *Chem. Eng. J.*, 2022, **449**, 137790.
110 F. Yang, Y. Zhao, Y. Du, Y. Chen, G. Cheng, S. Chen and W. Luo, *Adv. Energy Mater.*, 2018, **8**, 1703489.
111 H. Duan, D. Li, Y. Tang, Y. He, S. Ji, R. Wang, H. Lv, P. P. Lopes, A. P. Paulikas and H. Li, *J. Am. Chem. Soc.*, 2017, **139**, 5494–5502.
112 J. Yu, Y. Guo, S. She, S. Miao, M. Ni, W. Zhou, M. Liu and Z. Shao, *Adv. Mater.*, 2018, **30**, 1800047.
113 R. Wang, D. Li, T. Li, W. Sun and W. Hu, *Colloids Surf., A*, 2023, **668**, 131452.
114 K. C. Poon, D. C. Tan, T. D. Vo, B. Khezri, H. Su, R. D. Webster and H. Sato, *J. Am. Chem. Soc.*, 2014, **136**, 5217–5220.
115 F. Luo, Q. Zhang, X. Yu, S. Xiao, Y. Ling, H. Hu, L. Guo, Z. Yang, L. Huang and W. Cai, *Angew. Chem., Int. Ed.*, 2018, **57**, 14862–14867.
116 H. Xie, Q. Geng, X. Zhu, Y. Luo, L. Chang, X. Niu, X. Shi, A. M. Asiri, S. Gao and Z. Wang, *J. Mater. Chem. A*, 2019, **7**, 24760–24764.
117 H. Lv, Y. Teng, Y. Wang, D. Xu and B. Liu, *Chem. Commun.*, 2020, **56**, 15667–15670.
118 A. E. Henkes, Y. Vasquez and R. E. Schaak, *J. Am. Chem. Soc.*, 2007, **129**, 1896–1897.
119 M. Li, Y. Fang, G. Zhang, P. Cui, Z. Yang and J. He, *J. Mater. Chem. A*, 2020, **8**, 10433–10438.
120 G. Wu, X. Zheng, P. Cui, H. Jiang, X. Wang, Y. Qu, W. Chen, Y. Lin, H. Li and X. Han, *Nat. Commun.*, 2019, **10**, 4855.
121 G. Wu, X. Han, J. Cai, P. Yin, P. Cui, X. Zheng, H. Li, C. Chen, G. Wang and X. Hong, *Nat. Commun.*, 2022, **13**, 4200.
122 N. Yang, H. Cheng, X. Liu, Q. Yun, Y. Chen, B. Li, B. Chen, Z. Zhang, X. Chen and Q. Lu, *Adv. Mater.*, 2018, **30**, 1803234.
123 Q. Yao, Z. Yu, L. Li and X. Huang, *Chem. Rev.*, 2023, **123**, 9676–9717.
124 M. Wang, L. Li, M. Wang and X. Huang, *NPG Asia Mater.*, 2022, **14**, 78.
125 Y. Zhang, J. Fang, L. Zhang, D. Wei, W. Zhu and Z. Zhuang, *Chem. Commun.*, 2022, **58**, 4488–4491.
126 P. Li, W. Li, Y. Huang, J. Li, Q. Huang, S. Zhao and S. Tian, *Nanoscale*, 2022, **14**, 6258–6267.
127 Y. Xu, K. Ren, T. Ren, M. Wang, S. Yu, Z. Wang, X. Li, L. Wang and H. Wang, *J. Mater. Chem. A*, 2020, **8**, 19873–19878.
128 R. G. Chaudhuri and S. Paria, *J. Colloid Interface Sci.*, 2012, **369**, 117–122.
129 Y. Feng, Q. Yao, J. Li, N. Goswami, J. Xie and J. Yang, *Nano Res.*, 2016, **9**, 942–950.
130 C. Du, P. Li, F. Yang, G. Cheng, S. Chen and W. Luo, *ACS Appl. Mater. Interfaces*, 2018, **10**, 753–761.
131 R. Nandan and K. Nanda, *Nanoscale*, 2017, **9**, 12628–12636.
132 A. Li, J. Lin, Z. Huang, X. Wang and L. Guo, *iScience*, 2018, **10**, 1–10.
133 H. Gao, H. Zhou, Y. Hao, G. Zhou, H. Zhou, F. Gao, J. Xiao, P. Tang and G. Hao, *J. Semicond.*, 2023, **44**, 1–8.
134 Z. Fan, X. Zhang, J. Yang, X.-J. Wu, Z. Liu, W. Huang and H. Zhang, *J. Am. Chem. Soc.*, 2015, **137**, 10910–10913.
135 Y. Feng, Y. Ji, Y. Zhang, Q. Shao, Y. Xu, Y. Li and X. Huang, *Nat. Synth.*, 2022, **1**, 626–634.
136 D. Yoon, B. Seo, J. Lee, K. S. Nam, B. Kim, S. Park, H. Baik, S. H. Joo and K. Lee, *Energy Environ. Sci.*, 2016, **9**, 850–856.
137 J. Park, J. Park, J. Lee, A. Oh, H. Baik and K. Lee, *ACS Nano*, 2018, **12**, 7996–8005.
138 Y. Xu, C. Du, Q. Shen, J. Huang, X. Zhang and J. Chen, *Chem. Eng. J.*, 2021, **417**, 129318.
139 M. Xie, B. Zhang, Z. Jin, P. Li and G. Yu, *ACS Nano*, 2022, **16**, 13715–13727.
140 X. Zhang and G. Lu, *J. Phys. Chem. Lett.*, 2014, **5**, 292–297.
141 P. Moseley and W. A. Curtin, *Nano Lett.*, 2015, **15**, 4089–4095.
142 P. Strasser, S. Koh, T. Anniyev, J. Greeley, K. More, C. Yu, Z. Liu, S. Kaya, D. Nordlund, H. Ogasawara, M. F. Toney and A. Nilsson, *Nat. Chem.*, 2010, **2**, 454–460.
143 G. Meng, W. Sun, A. A. Mon, X. Wu, L. Xia, A. Han, Y. Wang, Z. Zhuang, J. Liu, D. Wang and Y. Li, *Adv. Mater.*, 2019, **31**, 1903616.
144 F. Shi, J. Peng, F. Li, N. Qian, H. Shan, P. Tao, C. Song, W. Shang, T. Deng, H. Zhang and J. Wu, *Adv. Mater.*, 2021, **33**, 2101511.
145 Y. Liu, Z. Chen, C. Liu, J. Zhang, W. Hu and Y. Deng, *J. Mater. Sci. Technol.*, 2022, **98**, 205–211.
146 J. Fan, Z. Feng, Y. Mu, X. Ge, D. Wang, L. Zhang, X. Zhao, W. Zhang, D. J. Singh, J. Ma, L. Zheng, W. Zheng and X. Cui, *J. Am. Chem. Soc.*, 2023, **145**, 5710–5717.
147 H. Guo, L. Li, Y. Chen, W. Zhang, C. Shang, X. Cao, M. Li, Q. Zhang, H. Tan, Y. Nie, L. Gu and S. Guo, *Adv. Mater.*, 2023, **35**, 2302285.

148 X. Guo, Z. Hu, J. Lv, H. Li, Q. Zhang, L. Gu, W. Zhou, J. Zhang and S. Hu, *Nano Res.*, 2022, **15**, 1288–1294.
149 L. Wang, Z. Zeng, W. Gao, T. Maxson, D. Raciti, M. Giroux, X. Pan, C. Wang and J. Greeley, *Science*, 2019, **363**, 870–874.
150 L. Sun and B. Liu, *Adv. Mater.*, 2023, **35**, 2207305.
151 Z. Li, X. Ai, H. Chen, X. Liang, X. Li, D. Wang and X. Zou, *Chem. Commun.*, 2021, **57**, 5075–5078.
152 H. Lv, L. Sun, D. Xu, W. Li, B. Huang and B. Liu, *CCS Chem.*, 2022, **4**, 2854–2863.
153 Y. Wang, L. Sun, H. Lv, C. Zheng and B. Liu, *CCS Chem.*, 2023, **5**, 1896–1907.
154 Y. Wang, H. Lv, L. Sun and B. Liu, *ACS Nano*, 2021, **15**, 18661–18670.
155 M. Zhao and Y. Xia, *Nat. Rev. Mater.*, 2020, **5**, 440–459.
156 X. Zhao, H. Cheng, X. Chen, Q. Zhang, C. Li, J. Xie, N. Marinkovic, L. Ma, J. C. Zheng and K. Sasaki, *J. Am. Chem. Soc.*, 2024, **146**, 3010–3022.
157 A. Mustafa, Y. Shuai, B. G. Lougou, Z. Wang, S. Razzaq, J. Zhao and J. Shan, *Chem. Eng. Sci.*, 2021, **245**, 116869.